

# Investigation of the structure, stability, and ionization dynamics of zirconium oxide clusters

M. Foltin, G. J. Stueber, and E. R. Bernstein

Citation: *The Journal of Chemical Physics* **114**, 8971 (2001); doi: 10.1063/1.1359177

View online: <http://dx.doi.org/10.1063/1.1359177>

View Table of Contents: <http://aip.scitation.org/toc/jcp/114/20>

Published by the American Institute of Physics

---

---

COMPLETELY  
REDESIGNED!



PHYSICS  
TODAY

*Physics Today* Buyer's Guide  
Search with a purpose.

# Investigation of the structure, stability, and ionization dynamics of zirconium oxide clusters

M. Foltin,<sup>a)</sup> G. J. Stueber, and E. R. Bernstein

*Department of Chemistry, Colorado State University, Fort Collins, Colorado 80523-1872*

(Received 13 December 2000; accepted 6 February 2001)

The growth dynamics, stabilities, and structures of small zirconium oxide clusters ( $Zr_nO_m$ ) are studied by covariance mapping time-of-flight mass spectrometry and density functional theory calculations. The zirconium oxide clusters are produced by laser ablation of zirconium metal into a helium gas flow seeded with up to 7% O<sub>2</sub>. The neutral ( $Zr_nO_m$ ) cluster distribution is examined at high and low ionization laser intensities. At high ionization laser intensities ( $\sim 10^7 \text{ W/cm}^2$ ) the observed mass spectra consist entirely of fragmented, nonstoichiometric clusters of the type  $[(ZrO_2)_{n-1}ZrO]^+$ , while in case of lower laser intensities ( $\sim 0.2 \times 10^7 \text{ W/cm}^2$ ), cluster fragmentation is strongly reduced and predominantly stoichiometric clusters  $(ZrO_2)_n^+$  appear. Under such gentle conditions,  $(ZrO_2)_5^+$  is found to be much more abundant than its neighboring clusters  $(ZrO_2)_n^+$ ,  $n = 1, 2, 4, 6, 7, 8$ . The unusually high signal intensity of the Zr<sub>5</sub>O<sub>10</sub><sup>+</sup> ion is found to be due to the high stability of the  $(ZrO_2)_5$  neutral cluster. Density functional theory calculations show a number of different conceivable isomer structures for this cluster and reveal the most likely growth pattern that involves the sequential uptake of ZrO<sub>2</sub> units by a  $(ZrO_2)_4$  cluster to yield  $(ZrO_2)_5$  and  $(ZrO_2)_6$ . Based on a series of different density functional theory and Hartree–Fock theory calculations, and on kinetic modeling of the experimental results, isomer structures, growth mechanisms, and stability patterns for the neutral cluster distribution can be suggested. The  $(ZrO_2)_5$  structure most stable at temperatures less than 3000 K is essentially a tetragonal pyramid with five zirconium atoms at the vertices, whereas an octahedral structure is the main building block of  $(ZrO_2)_6$ . Modeling of the covariance matrix over a wide range of ionization laser intensities suggests that  $(ZrO_2)_n$  neutral clusters absorb two photons of 193 nm radiation to ionize and then, for high laser intensity, the ion absorbs more photons to fragment. © 2001 American Institute of Physics. [DOI: 10.1063/1.1359177]

## I. INTRODUCTION

Catalytic activity of metal oxide particles and surfaces is generally not well understood. The properties that affect this reactivity include bonding character, ionicity (metal-to-oxygen charge transfer), oxidation numbers, and atomic coordination numbers, just to mention a few.<sup>1</sup> For small metal oxide clusters, bond character, ionicity, atomic oxidation, and coordination numbers can change significantly with cluster size. Therefore, a systematic study of small metal oxide cluster reactivity as a function of cluster size can yield insight into the role played by each of these properties in cluster reactivity. Such an investigation can partially discern which cluster property is rate determining and can generally contribute to the understanding of catalytic activity on a molecular level.<sup>2–4</sup>

To bring such a program to fruition, one first must understand how different cluster properties vary with cluster size. Spectroscopic studies can provide a wealth of information about cluster structure and bonding through the elucidation of cluster vibrations in photoelectron and infrared data,<sup>4(d),5</sup> however, such investigations seem only to be practical for small clusters. Near edge x-ray scattering (EXAFS)

is a promising technique for studying coordination environments of metal atoms in metal oxide clusters deposited on solid substrates, but the technical challenges involved in such experiments are considerable (e.g., high surface coverage and intense tunable x-rays).<sup>1</sup>

Analysis of “magic numbers”,<sup>3(a),3(b),5</sup> in the mass spectrum can often provide insights into the structural trends in cluster distributions. These “magic numbers” for the cluster distribution correspond to cluster ions with sizes  $n$  that appear with higher abundance than those with cluster sizes  $n-1$  and  $n+1$ . This approach is less direct than spectroscopy investigations because it relies on comparison of stabilities of cluster ions of different cluster sizes rather than on direct probing of molecular properties of the cluster of interest; however, unlike spectroscopic techniques [e.g., zero electron kinetic energy photoelectron spectroscopy (ZEKE), resonance enhanced multiphoton ionization (REMPI), mass resolved excitation spectroscopy (MRES),...], it is not limited to clusters of only small size. The “magic number” analysis method<sup>5</sup> has enabled understanding of the structural trends in van der Waals clusters, metal clusters, alkali oxide clusters, alkaline earth oxide clusters, as well as such new systems as C<sub>60</sub> and Ti<sub>8</sub>C<sub>12</sub>.

The analysis of “magic number” clusters in a mass spectrum is often complicated by the presence of cluster ion

<sup>a)</sup>Current address: Hewlett Packard Corporation, 3404 East Harmony Road, MS 32, Fort Collins, Colorado 80528.

fragmentation caused by excess energy deposited in a cluster in the ionization process.<sup>3</sup> Due to cluster ion fragmentation, the relationship between the measured cluster ion mass spectrum and the neutral cluster distribution can be obscured. The observed “magic numbers” can be due to stable neutral clusters, stable cluster ions (in the presence of fragmentation), or clusters with low ionization energy. Cluster ion fragmentation can, in principle, be suppressed by employing single photon, near threshold ionization. Ionization energies of metal oxide clusters are often above 8 eV; however, such radiation can be generated by tripling an UV laser in xenon, although tunability is a problem. Tunable radiation of greater than 8 eV can also be generated by synchrotrons. Photon fluxes at such energies are typically less than  $10^{12}$  photons/cm<sup>2</sup>/pulse. At such low light intensity, ion signals for clusters created by laser ablation may be too weak to detect under such circumstances. Moreover, since cluster ionization energies are expected to decrease with increasing cluster size, completely avoiding cluster fragmentation if all clusters must be ionized may not, in principle, be possible.

Many photon ionization with an UV laser (e.g., 193 nm) at photon energies lower than the cluster ion energy, should be more practical. Under these conditions, cluster ion fragmentation can be an imposing problem, especially if high ionization laser intensities are employed in order to increase ion signal intensities and the overall signal to noise ratio for the mass spectrum. Riley and co-workers studied ionization dynamics of several transition metal oxide clusters<sup>3</sup> under high ionization laser intensity conditions ( $>1\text{ J/cm}^2/10^{-8}\text{ s}$ ). They showed that, under these conditions, clusters can absorb up to 20 photons. Photoabsorption is followed by fast internal conversion (electronic to vibrational energy transfer) that leads to significant heating of the cluster, and eventual ionization by a process resembling thermionic emission. Similar observations have been made for several transition metal cluster systems, for C<sub>60</sub>, and for Ti<sub>8</sub>C<sub>12</sub>.<sup>4,5</sup> Cluster ions thereby produced are very hot and undergo extensive fragmentation.

This report suggests a new methodology to control cluster ion fragmentation. It is based on the following strategy.<sup>6</sup> First, record mass spectra at rather high ionization laser intensity (about  $100\text{ mJ/cm}^2/10^{-8}\text{ s}$ ) for which ion fragmentation is significant. Up to 2500 time-of-flight mass spectral scans are recorded at this laser intensity, and each scan is started by a single ionization laser pulse (10 Hz repetition rate). Second, measured mass spectra are evaluated for correlations between signal intensities of different mass peaks. Signal intensities in different mass channels or peaks (corresponding to cluster ions of different sizes  $n$ ) are slightly different in each individual scan because of small pulse-to-pulse fluctuations of the ionization laser intensity. The collected correlations are organized into a so-called covariance matrix. Third, measured covariance matrices are fitted by a simple theoretical algorithm of the cluster ion fragmentation. This model includes a number of fitting parameters—absorption cross sections, cluster ionization energy, cluster dissociation energy, etc. A number of possible combinations of fitting parameters fit both the measured mass spectral cluster ion distributions and the measured normalized covari-

ances. An extensive search of the entire parameter space is executed. Fourth, for each combination of fitting parameters, the value of the ionization laser intensity that reduces fragmentation below some predetermined lower limit is simulated. The most conservative lower limit of laser intensity is found for the parameter space. Fifth, the mass spectrum is recorded at this low ionization intensity at which cluster fragmentation is expected to be negligible. The intensity variation in the measured cluster ion distribution (i.e., the “magic numbers”) obtained at this low laser intensity should correspond to intensity variations in the neutral cluster distribution.

This procedure is possible because covariance is a measure of cluster fragmentation, as the parent and fragment ion signal intensities are correlated. The covariances between parent ion and fragment ion are negative because the fragment is formed at the expense of the parent. In reality, however, the covariances follow a much more complicated relationship that results from changes in both ionization probability and fragmentation probability with pulse-to-pulse fluctuations of the ionization laser intensity. Detailed theoretical modeling is required to express this relationship between experimental variables and the covariance matrix for a sample of clusters. For example, parent ion/fragment ion covariances change from negative to positive as the ionization laser intensity is decreased while fragmentation is still observed. Upon further decrease of the ionization laser intensity, the covariances finally become small and positive as the fragmentation disappears. Both experiments and theoretical modeling support this trend.

In this work, the structural trends in zirconium oxide clusters are explored. Zirconium oxide can serve as a high temperature structural ceramic and as a catalyst for dehydrogenation of hydrocarbons. Following the methodology described above, the mass spectrum of (ZrO<sub>2</sub>)<sub>*n*</sub> cluster ions is recorded at very low ionization laser intensities at which cluster fragmentation due to the ionization process is negligible. The mass spectrum shows a very prominent “magic number” at cluster size  $n=5$ . The intense ion peak in the mass spectrum can be related to an exceptional stability of the (ZrO<sub>2</sub>)<sub>5</sub> neutral cluster. (ZrO<sub>2</sub>)<sub>*n*</sub> cluster ions with cluster sizes  $n=3,4,6,7$  have very small ion signals in the zirconium oxide mass spectrum. For  $12\geq n\geq 8$ , the cluster ion intensities are again high and reach intensity levels close to the (ZrO<sub>2</sub>)<sub>5</sub> cluster ion intensity.

The structures and stabilities of (ZrO<sub>2</sub>)<sub>*n*</sub>,  $n=3-6$ , neutral clusters are calculated using density functional theory and Hartree–Fock theory. Geometry optimizations with full relaxation of all coordinates are done on several of the calculated isomers for these clusters in an attempt to find the global minimum on the cluster potential hypersurface of each cluster size. The selected levels of theory predict that (ZrO<sub>2</sub>)<sub>5</sub> is more stable than (ZrO<sub>2</sub>)<sub>3</sub>, (ZrO<sub>2</sub>)<sub>4</sub>, and (ZrO<sub>2</sub>)<sub>6</sub> in agreement with experiments. The most stable (ZrO<sub>2</sub>)<sub>5</sub> isomer is neither very symmetric nor exceptionally compact. A clear structural building pattern is observed between the most stable isomers of (ZrO<sub>2</sub>)<sub>4</sub> and (ZrO<sub>2</sub>)<sub>5</sub> and the second most stable isomer of (ZrO<sub>2</sub>)<sub>6</sub>. These three clusters have a common basic building block—the tetrahedral (ZrO<sub>2</sub>)<sub>4</sub> clus-

ter with four zirconium atoms at the apices of the tetrahedron, six oxygen atoms along the tetrahedron edges, and two dangling terminal oxygen atoms each connected to a single zirconium atom. Closer analysis reveals that the  $(\text{ZrO}_2)_5$  special stability results from the interplay between reducing the number of singly bonded oxygen atoms of  $(\text{ZrO}_2)_4$  and increasing the strain of deformation of the  $(\text{ZrO}_2)_4$  building block as the cluster size increases from  $n=4$  to  $n=6$ . The most stable isomer of the  $(\text{ZrO}_2)_6$  cluster has a very different structure. This structure appears to begin a new building pattern at the  $n=6$  cluster that reaches high stability at  $n=8$  or 9. These different structural patterns may exhibit different reactivities due to different coordination numbers for oxygen atoms.

The simulation of cluster growth, fragmentation, and the covariance matrix suggests that neutral zirconium oxide clusters absorb two photons to ionize and then, if the ionization laser intensity is high enough, the parent cluster ion absorbs several more photons and accumulates sufficient energy to fragment. At low ionization laser intensity, parent ion fragmentation can be reduced to negligible levels.

## II. EXPERIMENTAL PROCEDURES

A conventional laser vaporization/supersonic expansion cluster source is used to generate the neutral zirconium oxide clusters by laser ablation of zirconium metal into helium carrier gas mixed with up to 7% of O<sub>2</sub>. The pulsed helium/oxygen flow from an R. M. Jordan Co. pulsed valve operating at backing pressure 100 psi is injected through 0.8 mm diam nozzle orifice into a 2 mm diam, ~60 mm long flow channel in the laser ablation source. The zirconium is ablated by a 532 nm laser beam (second harmonic of a Nd/YAG laser at laser energies of ~2 to 20 mJ/pulse) directed perpendicularly to the carrier gas channel and focused with a  $f = 100$  cm lens on the surface of a rotating and translating drum wrapped with a 0.1 mm thick zirconium metal foil (99.98%).

The sample surface is tangential to the flow channel wall and the ablation spot is approximately 27.5 mm downstream from the nozzle orifice. About 32.5 mm downstream from the ablation spot, the clusters seeded in the carrier gas expand into the vacuum. The neutral clusters of this resulting molecular beam pass through a 1.1 mm skimmer into the ion source of a time-of-flight mass spectrometer (TOF; Wiley-McLaren-type) where their flow is intersected, and they are ionized by an ArF (193 nm) excimer laser beam ( $\sim 10^{-8}$  s pulse duration). The generated cluster ions are extracted perpendicularly to the molecular beam and enter a 1.8 m long flight tube. They are separated in arrival time according to their masses (ions have 4 keV kinetic energy) and detected by Galileo microchannel plate detector. Signals from the detector are fed to a Tektronix RTD 720A transient digitizer. Signal sampling, processing procedures and mathematical techniques are identical to those described previously.<sup>6</sup>

In most cases, the mass spectral data are recorded with a focused ionization laser beam utilizing laser fluences from 20 to 200 mJ/cm<sup>2</sup>. The laser fluence is determined by dividing the laser beam radiant energy measured with a Moletron J-25 pyroelectric probe with the laser beam area measured at

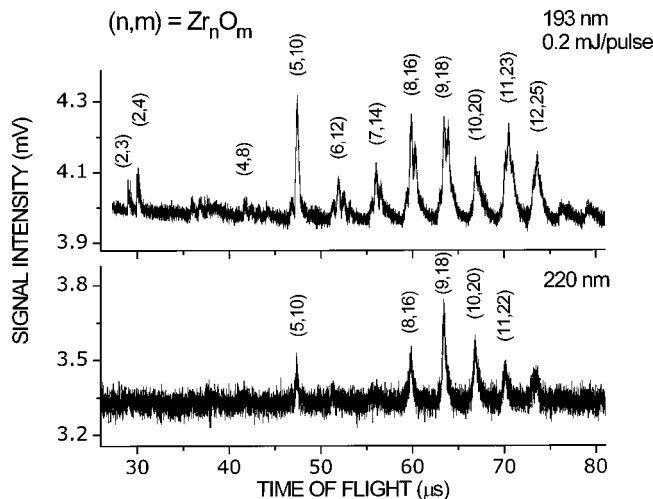


FIG. 1. The mass spectra of  $\text{Zr}_n\text{O}_m$  clusters recorded at low ionization laser intensities ( $\sim 0.20$  mJ/pulse, pulselength  $\sim 10^{-8}$  s, area  $= 9 \times 10^{-3} \text{ cm}^2$ ,  $I \sim 0.2 \times 10^7 \text{ W/cm}^2$  at 193 nm (6.43 eV, upper trace) and 220 nm (5.64 eV, lower trace). For each  $n$ , only the most intense  $\text{Zr}_n\text{O}_m$  peak is labeled as  $(n,m)$ . Note that in the upper trace the mass peaks for  $n > 5$  are split. The satellite peaks adjacent to the labeled mass peaks correspond to clusters with one extra oxygen atom. For example, the high mass satellite of (6, 12) is (6, 13). These peaks disappear upon reducing the oxygen concentration and pulse valve current.

the ionization spot (note that the excimer laser beam intensity profile is roughly rectangular). The laser beam radiant energy is varied between 0.2 and 2 mJ. The area of a tightly focused ionization laser beam is  $0.9 \text{ mm}^2$  ( $3 \text{ mm} \times 0.3 \text{ mm}$ ; size of the laser beam induced burn mark on photographic paper measured under a microscope).

## III. EXPERIMENTAL RESULTS AND ANALYSIS

Figure 1 shows the mass spectrum of  $\text{Zr}_n\text{O}_m$  clusters recorded at two different ionization laser wavelengths, 193 nm (6.43 eV) and 220 nm (5.64 eV), and at slightly different expansion conditions (O<sub>2</sub> concentrations and nozzle opening times). The background noise level in these spectra is rather high as the spectra are recorded at very low ionization laser intensities to minimize cluster ion fragmentation. The mass peaks are relatively broad due to Zr atom natural isotopic distribution, and individual isotopic features are resolved for only  $(\text{ZrO}_2)_n$ ,  $n \leq 3$ .  $\text{Zr}_n\text{O}_m$  clusters with different numbers of oxygen atoms  $m$  for a given number  $n$  of Zr atoms can be resolved up to cluster size  $n=12$ , even at these low signal intensity levels. The prominent features in the spectra of Fig. 1 correspond to a progression of  $(\text{ZrO}_2)_n^+$  cluster ions. The spectrum recorded with 193 nm ionization laser wavelength also shows oxygen rich  $(\text{ZrO}_2)_n\text{O}^+$ ,  $n > 5$ , cluster ions. Intensities for oxygen rich clusters ion peaks are low for small clusters but become larger for clusters with  $n > 10$ . The oxygen rich clusters disappear upon slight changes in the expansion conditions.

Despite the fact that the two cluster ion distributions shown in Fig. 1 are different, one can clearly discern a number of important common trends in these cluster ion distributions: (1) signal intensities of small cluster ions,  $(\text{ZrO}_2)_3^+$

and  $(\text{ZrO}_2)_4^+$ , are low; (2)  $(\text{ZrO}_2)_5^+$  cluster ion signal intensity is very high relative to that of its neighboring peaks; (3)  $(\text{ZrO}_2)_6^+$  and  $(\text{ZrO}_2)_7^+$  cluster ion signal intensities are low; and (4)  $(\text{ZrO}_2)_n^+$ ,  $8 \leq n \leq 12$ , signal intensities are again relatively high. In short,  $(\text{ZrO}_2)_5^+$  is a “magic number” in the mass spectrum of  $(\text{ZrO}_2)_n$  clusters, and gaps exist in the mass spectrum between  $(\text{ZrO}_2)_2^+$  and  $(\text{ZrO}_2)_5^+$  and between  $(\text{ZrO}_2)_5^+$  and  $(\text{ZrO}_2)_8^+$ . Additionally, the mass peaks from  $8 \leq n \leq 12$  become intense and appear as a new set of “magic numbers.”

What is the nature of the  $(\text{ZrO}_2)_5^+$  “magic number” cluster and what is the nature of the second “magic number” cluster set ca.  $(\text{ZrO}_2)_n^+$ ,  $8 \leq n \leq 12$ ? In general, the cluster ion  $X_n^+$  can be “magic” in the mass spectrum (that is, apparently much more abundant than its neighbors) for one of three reasons: (1) ionization efficiency of the  $X_n$  neutral cluster is higher than that of its neighbors  $X_{n-1}$  and  $X_{n+1}$  in the neutral cluster distribution; (2) clusters undergo fragmentation following ionization, and cluster ion  $X_n^+$  is thermodynamically more stable than the cluster ions  $X_{n-1}^+$  and  $X_{n+1}^+$ ; and (3) neutral cluster  $X_n$  is very abundant in the neutral cluster distribution due to its high thermodynamic stability compared to that of its neighboring cluster sizes,  $X_{n-1}$  and  $X_{n+1}$ .

In the ensuing sections, these three possibilities for  $(\text{ZrO}_2)_n^+$  “magic number” clusters will be thoroughly examined. The remainder of the presentation in this report is devoted to determining the source of this cluster ion distribution. We finally come to the conclusion that the cluster ion distribution measured in Fig. 1 is indicative of the neutral cluster distribution and that  $(\text{ZrO}_2)_n^+$ ,  $n=5$ , 8–12, are “magic numbers” for the neutral cluster distribution. The  $(\text{ZrO}_2)_n$  structural trends and the origins of the special stability of the  $(\text{ZrO}_2)_5$  cluster are explored in Sec. IV.

### A. Cluster ionization dynamics

Even at the relatively short ionization wavelengths employed in these studies, the photon energy is not high enough to ionize the  $(\text{ZrO}_2)_n$  clusters by single photon ionization. Clusters are ionized by a multiphoton process that is either non-resonant or resonantly enhanced for the first photon absorption. In general, for metal and metal oxide clusters with cluster size  $n > 3$ , densities of states above the first excited state are high. Thus, the energy level of the first absorbed photon for multiphoton ionization may well be in resonance with other vibronic excited states located within a dense manifold of states. The probabilities for intersystem crossings and/or internal conversions between different excited states, and of energy flow from one state to another and ultimately to vibrations, are thus, very high. Hence, the (non-radiative) lifetimes of these excited states are usually short ( $< 1$  ps) compared to the 10 ns ionization laser pulse duration, and cluster ionization competes with internal conversion. This latter process, radiationless relaxation of the photoaccessed state at constant cluster energy, thus heats the cluster. Subsequent cluster ionization under the above circumstances can occur in two different regimes: (1) a neutral cluster absorbs so many photons (at high laser intensity) that it becomes very hot and emits and electron by thermionic

emission (i.e., rapid redistribution of energy in the cluster),<sup>3(a)–3(c),4(g),7</sup> or (2) a neutral cluster absorbs only a few photons (low laser intensity) and ionizes as the total electronic excitation energy in the cluster exceeds the cluster ionization threshold (e.g., slow redistribution of energy in the neutral cluster).<sup>4(g)</sup>

Ionization studies on various transition metal and metal oxide clusters (Ref. 2), and  $\text{Ti}_8\text{C}_{12}$ , and  $\text{C}_{60}$  clusters show that, at very high laser fluence ( $> 100 \text{ mJ/cm}^2$ ), the dominant ionization channel involves absorption of many photons by the neutral cluster, leading to heating of the cluster and subsequent ionization by a process similar to thermionic emission from a solid surface. This is a realization of regime 1 above. In this regime, ion signal intensity scales with a very high power of the ionization laser intensity ( $n > 9$  for vanadium oxide, iron oxide, chromium oxide clusters<sup>3(a)</sup>) suggesting absorption of many photons. The many photon absorption is explained by a cycling of the cluster between the ground electronic state (or some low lying excited state) and some higher electronic excited state through a sequence of many photon absorption/internal conversion steps that leaves the system highly vibrationally excited (hot). The cluster ionization efficiency is then very sensitive to the cluster ionization energy because the probability of thermionic emission scales exponentially with ionization energy.<sup>3,4</sup> In such instances, cluster ions undergo extensive fragmentation.

At the low laser fluences ( $\leq 20 \text{ mJ/cm}^2$ ) used to record the mass spectra shown in Fig. 1, cluster ionization occurs in the second regime described above. Signal intensity scales with a low power of the ionization laser intensity (approximately 2.15 in the present case). This dependence suggests that only a few photons (2 or 3) are absorbed by the cluster prior to ionization (*vide infra*). This regime is similar to that for multiphoton ionization of simple small molecules. Evidently, much less energy is lost to the vibrations than in the foregoing ionization regime 1. Those neutral clusters that lose energy to vibrations (due to internal conversion) following absorption of the first/second photon will not be ionized at such low laser intensities as the number of photons absorbed is too low to heat the cluster hot enough for thermionic emission to occur. Vanadium oxide and titanium oxide clusters are also ionized by this mechanism at low laser intensities.<sup>6(a)</sup>

Mass spectra of  $(\text{ZrO}_2)_n$  cluster ions are recorded at two different ionization laser wavelengths to exclude the possibility that one wavelength accidentally is in resonance with a long-lived ( $\sim 1$  ns) excited state of  $(\text{ZrO}_2)_5$ . This circumstance would enhance the  $(\text{ZrO}_2)_5$  ionization efficiency compared to that of other clusters due to resonantly enhanced multiphoton ionization. Nonetheless,  $(\text{ZrO}_2)_5^+$  is “magic” (high signal intensity) at both 193 and 220 nm ionization laser wavelengths (see Fig. 1). Thus, the special nature of  $(\text{ZrO}_2)_5^+$  is not associated with a special ionization cross section at the chosen laser wavelength [i.e., an accidental resonance with a long-lived intermediate excited state of  $(\text{ZrO}_2)_5$ ].

The possibility that the  $(\text{ZrO}_2)_5$  clusters are ionized by a lower number of photons than clusters of the other sizes can also be excluded. Figure 2 shows the dependence of the

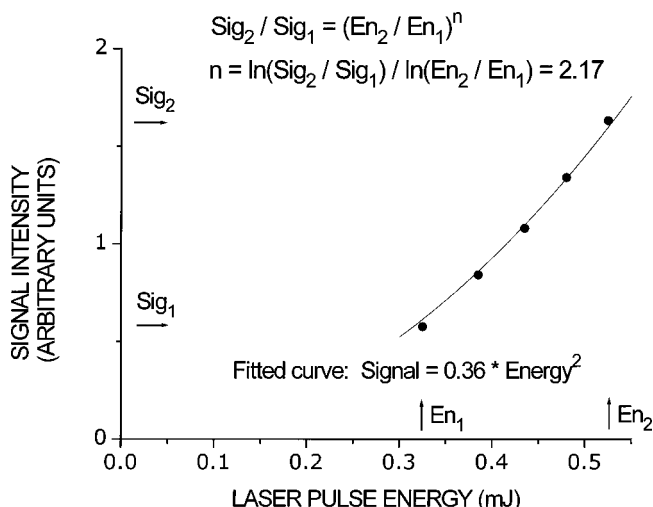


FIG. 2. Dependence of the  $(\text{ZrO}_2)_5^+$  signal intensity on the ionization laser energy at 193 nm ionization laser wavelength.

$(\text{ZrO}_2)_5^+$  signal intensity on ionization laser energy/pulse recorded at 193 nm laser wavelength. The  $(\text{ZrO}_2)_5^+$  signal intensity increases with the power 2.15 of the laser energy/pulse, which suggests that  $(\text{ZrO}_2)_5$  is ionized by a two or possible three photon ionization process at 193 nm. This suggests that the ionization energy (IE) for  $(\text{ZrO}_2)_5$  is  $6.43 \leq \text{IE} \leq 12.86$  or 19.29 eV. Ionization energies of the clusters will surely be lower than 12.86 eV, because the ionization energy of  $\text{ZrO}_2$  is 9.5 eV. Thus,  $(\text{ZrO}_2)_{3,4,6,7,\dots}$  clusters should be ionized by two photons of 193 nm laser energy, as well.

Hence, the ionization efficiency of the  $(\text{ZrO}_2)_5$  clusters should be comparable to the ionization efficiencies of the neighboring clusters ( $n=4$  and 6) and the “magic” character of  $(\text{ZrO}_2)_5^+$  mass spectral feature is not caused by an enhanced ionization efficiency of the  $(\text{ZrO}_2)_5$  clusters compared to other cluster sizes.

## B. Cluster ion fragmentation

Under multiphoton ionization conditions (high laser fluence and the requirement that one photon energy is insufficient to ionize the clusters, in general), cluster ion fragmentation can be an important and nagging issue. Three arguments can be proffered in support of the conclusion that at an ionization laser wavelength of 193 nm and at low ionization laser energy and fluence ( $\sim 0.20$  mJ/pulse,  $\sim 21$  mJ/cm $^2$ /pulse,  $0.2 \times 10^7$  W/cm $^2$ ) (see Fig. 1), cluster ion fragmentation is absent or minimal.

The first evidence against cluster ion fragmentation under these circumstances comes from observed trends in the ionization laser intensity dependence of cluster ion stoichiometries. At high ionization laser energies ( $\sim 1$  mJ/pulse,  $\sim 110$  mJ/cm $^2$ /pulse), mass spectra consist of only nonstoichiometric, metal rich cluster ions  $(\text{ZrO}_2)_{n-1}\text{ZrO}^+$  (see Fig. 3). At low ionization laser energies ( $\sim 0.20$  mJ/pulse), metal rich cluster ions completely disappear from the mass spectra of  $(\text{ZrO}_2)_n$  clusters, which is now composed of only stoichiometric  $(\text{ZrO}_2)_n^+$  cluster ions, as shown in Fig. 1.

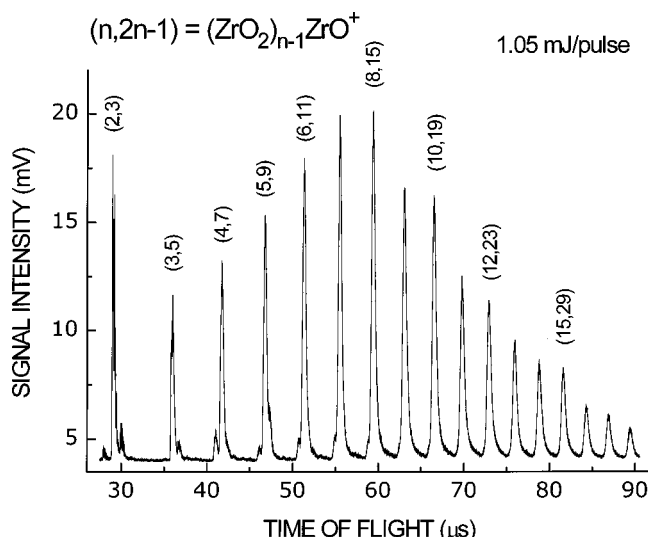


FIG. 3. The mass spectrum of  $\text{Zr}_n\text{O}_m$  clusters recorded at high ionization laser intensity ( $I \sim 10^7$  W/cm $^2$ ) at 193 nm laser wavelength. Note that at this intensity the mass spectrum consists of only the nonstoichiometric, metal-rich cluster ions  $(\text{ZrO}_2)_{n-1}\text{ZrO}^+$ .

Evidently, at high ionization laser intensity ( $>75$  mJ/cm $^2$ /pulse) cluster ions undergo fragmentation. Nonstoichiometric  $(\text{ZrO}_2)_{n-1}\text{ZrO}^+$  cluster ions arise from stoichiometric  $(\text{ZrO}_2)_{n+d}^+, d \geq 0$ , cluster ions by the loss of an oxygen atom and  $d$   $\text{ZrO}_2$  molecules [or a  $\text{ZrO}_3$  molecule and  $(d-1)$   $\text{ZrO}_2$  molecules]. At low ionization laser intensities, oxygen (or  $\text{ZrO}_3$ ) evaporation is not present; under these conditions, evaporation of  $\text{ZrO}_2$  molecules will also be absent, unless the  $\text{ZrO}_2$  evaporation channel has lower activation energy (or higher activation entropy) than the oxygen evaporation channel. If the latter were the case, however, sequential evaporation of  $\text{ZrO}_2$  units would quickly cool the cluster and the oxygen (or  $\text{ZrO}_3$ ) evaporation channel would be only a minor one, also at high ionization laser intensities. Thus, at low ionization laser intensity, the loss of  $\text{ZrO}_2$  moieties is not likely.

The second argument against cluster ion fragmentation at low ionization laser fluence comes from calculation of  $\text{ZrO}_2$  evaporation probability for the upper limit of internal energy deposited in the cluster. The internal energy distribution in the cluster deposited from the ionization processes is estimated from the measured laser intensity dependence of the  $(\text{ZrO}_2)_5^+$  cluster signal intensity. Assume for the moment that the  $(\text{ZrO}_2)_5^+$  cluster ion is produced by ionization and fragmentation of  $(\text{ZrO}_2)_6$  or some larger neutral parent cluster  $(\text{ZrO}_2)_{5+d}$  ( $d > 0$ ). As shown in Fig. 2, the  $(\text{ZrO}_2)_5^+$  signal increases with the 2.15 power of laser energy. Hence, the  $(\text{ZrO}_2)_{5+d}$  neutral precursor of  $(\text{ZrO}_2)_5^+$  undergoes absorption of two or possible three photons at 193 nm. Thus, the energy deposited in the  $(\text{ZrO}_2)_{5+d}$  cluster in the ionization is, at most, 19.29 eV.

To this energy must be added the internal (thermal) energy of the neutral cluster prior to ionization. In our previous work on vanadium oxide and titanium oxide clusters carried out under very similar conditions,<sup>6(a)</sup> cluster temperature in the molecular beam is estimated by measuring mass resolved

excitation spectra of the VO molecule of the  $\text{VO}(A \leftarrow X)$  electronic transition.<sup>8</sup> The vibrational temperature of VO obtained by comparing intensities for the  $(1 \leftarrow 0)$  and  $(1 \leftarrow 1)$  vibronic transitions is about  $T_{\text{vib}} \sim 950 \pm 100$  K. Larger clusters are expected to have lower  $T_{\text{vib}}$  because their low frequency “phonon” modes will be cooled more efficiently in collisions with the expansion gas. Hence, for this argument,  $T = 950$  K is taken as an (extreme) upper limit for the neutral cluster thermal energy. Note, too, that Hackett and co-workers,<sup>4(e),4(g)</sup> assume that metal oxide, carbide, and nitride clusters have an internal temperature equal to the internal temperature of the laser ablation source block ( $T_{\text{source}} \sim 300$  K).

Based on the vibrational analysis of the most stable conformer of  $(\text{ZrO}_2)_6$  [see next section for the *ab initio* calculation of  $(\text{ZrO}_2)_n$  cluster structure], about 73% of all vibrational modes of  $(\text{ZrO}_2)_6$  will be populated at this temperature. Such a set of assumptions gives  $(\text{ZrO}_2)_6$  internal vibrational energy at ca. 2.88 eV. Thus, the upper limit to the total internal energy of  $(\text{ZrO}_2)_6^+$  following ionization of neutral  $(\text{ZrO}_2)_6$  is ca. 22.2 eV.

Part of this energy is needed to ionize the cluster. We are certain that the  $(\text{ZrO}_2)_n$  ( $n < 20$ ) clusters studied in this work cannot be ionized by a single-photon ionization. Cluster signal intensities decrease significantly upon defocusing of the ionization laser beam and no clusters are observed with a completely unfocused laser beam. This is in contrast to the ionization behavior of the metal rich vanadium oxide and titanium oxide clusters that we studied previously.<sup>6(a)</sup>  $(\text{ZrO}_2)_n$  clusters need to absorb more photons than  $(\text{VO}_2)_p(\text{VO})_q$  and  $(\text{TiO}_2)_p(\text{TiO})_q$  clusters to be ionized. Based on our *ab initio* calculations (*vide infra*), the adiabatic ionization energy for the  $(\text{ZrO}_2)_6$  cluster is about 8.5 eV; note that this is lower than the ionization energy of the  $\text{ZrO}_2$  molecule,<sup>9</sup> as expected. Then, the upper limit for the internal energy of the  $(\text{ZrO}_2)_6^+$  cluster ion that is available for the fragmentation is  $22.17 - 8.5 = 13.67$  eV.

Based on *ab initio* calculations reported below, the binding energy,  $E_d$ , of  $\text{ZrO}_2$  in  $(\text{ZrO}_2)_6$  is at least 4.35 eV. If one assumes that the  $\text{ZrO}_2$  binding energy in  $(\text{ZrO}_2)_6^+$  is about the same, the fragmentation rate  $k$  for the reaction,



can be estimated based on the RRK formula,

$$k = k_0(1 - E_d/E)^{s-1} \quad (2)$$

in which  $k_0$  is related to the effective vibrational frequency for the reaction coordinate,  $s = 48$  is the number of vibrational modes of the cluster  $(\text{ZrO}_2)_6^+$ , and  $E$  is the internal energy of the  $(\text{ZrO}_2)_6^+$  cluster ion. Assuming  $k_0 = 10^{13} \text{ s}^{-1}$  and  $E = 13.67$  eV,  $k = 1 \times 10^5 \text{ s}^{-1}$ . The number of  $N_f$  of  $(\text{ZrO}_2)_6^+$  cluster ions that undergo fragmentation within the ion sources of the time-of-flight mass spectrometer can then be expressed as

$$N_f = N(0)(1 - e^{-kt}) \quad (3)$$

in which  $t = 1.5 \times 10^{-6}$  s is the residence time of the  $(\text{ZrO}_2)_6^+$  ion in the source region and  $N(0)$  is the number of  $(\text{ZrO}_2)_6^+$  cluster ions produced. Substituting  $k = 1 \times 10^5 \text{ s}^{-1}$  in Eq. (3)

yields  $N_5(t)/N(0) \sim 0.14$ . Thus, less than 15% of the  $(\text{ZrO}_2)_6^+$  cluster ions undergo fragmentation reaction Eq. (1) under these assumed conditions. The ratio of the fragment and parent ion intensities,  $N_f(t)/N(t) = N_f(t)/[N(0) - N_f(t)] \sim 0.17$  is negligibly small. As given in Fig. 1, the  $(\text{ZrO}_2)_5^+$  cluster ion signal intensity is more than 250% of the  $(\text{ZrO}_2)_6^+$  signal intensity and more than 150% of the sum of the  $(\text{ZrO}_2)_6^+$  and  $(\text{ZrO}_2)_6\text{O}^+$  cluster ion signal intensities.

The weakness of this second argument and analysis for the absence of cluster ion fragmentation at low ionization laser intensity is that it is based on theoretical calculations of cluster ionization energy (IE) and dissociation energy ( $E_d$ ). Experiments give only a lower bound for the ionization energy of 6.43 eV. To be more conservative, this latter value of IE could be employed in the calculation of cluster ion fragmentation.

The third argument against cluster ion fragmentation giving rise to the cluster ion distribution depicted in Fig. 1, rather than this distribution reflecting the neutral  $(\text{ZrO}_2)_n$  cluster distribution, can be found in the covariance mapping results for the  $(\text{ZrO}_2)_n^+$  cluster ion mass spectral data. These data are presented and analyzed in the following subsection. Covariance mapping of the mass spectra, in conjunction with covariance simulations, yields a tighter bound on the upper limit of the internal energy of the cluster ion at a given ionization laser intensity. Simulation of these results allows the parameters IE and  $E_d$  to be varied over a wide range of values and the highest fragmentation probability can be employed to generate the most conservative estimate of cluster fragmentation. The essence of this approach is twofold: (1) obtain all permissible combinations of parameters IE and  $E_d$  that will fit the measured covariance matrix at high ionization laser intensity for which cluster fragmentation is dominant; and (2) predict how much the laser intensity must be decreased so that the maximum fragmentation possibility over all permissible combinations of IE and  $E_d$  becomes negligible. Following this procedure in the next subsection of this paper, will provide the third and strongest evidence against cluster ion fragmentation at the low laser intensity employed to record the mass spectra displayed in Fig. 1.

### C. Covariance mapping of the mass spectra: Results and simulations

Before presenting experimental covariance maps as a function of laser fluence at 193 nm ionization photon wavelength, we motivate these studies by a description of the covariance matrix and a discussion of what to expect for covariance data taken at high laser fluence. This situation reflects the experimental conditions leading to significant cluster ion fragmentation.

The neutral cluster distribution can be pictured as a collection of clusters of different sizes  $n$ . If the initial cluster ion undergoes fragmentation,



fluctuations of the  $(\text{ZrO}_2)_n^+$  parent ion signal, and of the  $(\text{ZrO}_2)_{n-d}^+$  fragment ion signal should be correlated since both ions arise from the same neutral cluster size  $n$ . Neutral clusters should, in turn, be correlated by the cluster growth

process. Correlations between signal intensities of different cluster ion peaks can be easily measured by time-of-flight mass spectrometry. A complete time-of-flight mass spectrum can be recorded from a single ionization laser pulse. Typically, 2500 single laser pulse mass spectra are recorded and evaluated for correlations between different cluster ion features. Correlations are plotted in the form of a covariance matrix.

The sign and magnitude of the parent/fragment ion correlation depend upon the character of the prevailing fluctuations. For example, in our recent study of toluene/water, aniline/argon, and fluorostyrene/argon clusters, the clusters are ionized by two-color, two-photon resonant ionization.<sup>6(a)</sup> Since the number of absorbed photons is independent of the ionization laser intensity, in general, the correlations are not affected by laser intensity fluctuations. Neutral cluster intensity fluctuations of the number of clusters at cluster size  $n$  prevail in this latter instance, and parent ion/fragment ion corrections are found to be small and positive.<sup>6(b)</sup> Vanadium oxide and titanium oxide clusters also have small positive covariance matrix elements that are laser intensity independent and neutral cluster growth derived.<sup>6(a)</sup> Conversely, for zirconium oxide neutral clusters ionized by one-color, many photon ionization (high laser fluence), the number of absorbed photons is a very sensitive function of the laser intensity. Laser intensity fluctuations leading to fluctuations of the number of absorbed photons on a pulse-to-pulse basis prevail, and parent ion/fragment ion correlations are negative.

To demonstrate the effect of laser intensity fluctuation on the covariance matrix for  $(\text{ZrO}_2)_n^+$  clusters, results of simulations of cluster ion fragmentation at high ionization laser intensities ( $\sim 1 \times 10^7 \text{ W/cm}^2$ ,  $\sim 1 \text{ mJ/pulse}$ ,  $\sim 100 \text{ mJ/pulse/cm}^2$ ) are presented. The details of the simulation are given below. Figure 4 shows the photoabsorption probability distributions for  $(\text{ZrO}_2)_{10}$  clusters as a function of the number  $m$  of absorbed photons plotted for ionization laser intensities  $I$ ,  $I - 3\sigma$ , and  $I + 3\sigma$ , for which  $I \sim 1 \times 10^7 \text{ W/cm}^2$ , and  $\sigma = 5\% I$  is the standard deviation of the laser intensity distribution measured for the ionization laser employed. Assuming a normal distribution of laser intensity fluctuations, 99.7% of all laser pulses will have intensities within the confidence interval  $\langle I - 3\sigma, I + 3\sigma \rangle$ . Hence,  $I - 3\sigma$  and  $I + 3\sigma$  can be accepted as good lower and upper bounds, respectively, for fluctuating laser intensities. For  $(\text{ZrO}_2)_{10}$ , the photoabsorption distribution shifts by more than 2 photons between  $I - 3\sigma$  and  $I + 3\sigma$ : at laser intensity  $I - 3\sigma$ , 8 photons are absorbed by  $(\text{ZrO}_2)_{10}$  with highest probability, and at laser intensity  $I + 3\sigma$ , 10 photons are absorbed by  $(\text{ZrO}_2)_{10}$  with highest probability. Assuming that the activation energy for  $\text{ZrO}_2$  evaporation from  $(\text{ZrO}_2)_{10}$  is  $E_d = 6 \text{ eV}$ , the  $(\text{ZrO}_2)_{10}$  ionization energy is  $\text{IE} = 8 \text{ eV}$ , and the  $(\text{ZrO}_2)_{10}$  neutral cluster temperature is  $T = 950 \text{ K}$ , the RRK formula Eq. (2) predicts that  $(\text{ZrO}_2)_{10}$  must absorb more than five photons to evaporate the first  $\text{ZrO}_2$  monomer within  $1 \mu\text{s}$  after ionization.

Variation in the number of absorbed photons for  $(\text{ZrO}_2)_n$  clusters will lead to variations in the fragmentation and ionization probabilities. In this discussion, the product of ionization and fragmentation probabilities are combined into a

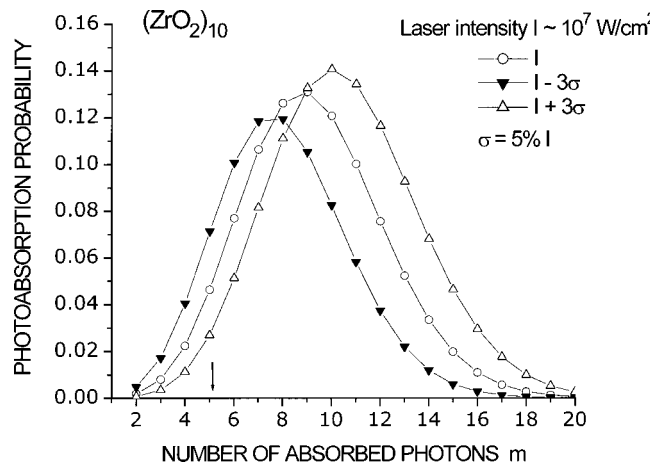


FIG. 4. The photoabsorption probability distributions of the  $(\text{ZrO}_2)_{10}$  clusters as functions of the number  $m$  of absorbed photons calculated by formula (14) and plotted for ionization laser intensities  $I$ ,  $I - 3\sigma$ , and  $I + 3\sigma$ ,  $I \sim 10^7 \text{ W/cm}^2$  and  $\sigma = 5\% I$  is the standard deviation of the laser with intensity distribution measured for our ionization laser. Note that assuming a Gaussian distribution of laser intensity fluctuations, 99.7% of all laser pulses will have intensities within the confidence interval  $\langle I - 3\sigma, I + 3\sigma \rangle$ . The vertical arrow shows how many photons need to be absorbed by  $(\text{ZrO}_2)_{10}$  to evaporate the first  $\text{ZrO}_2$  monomer within  $1 \mu\text{s}$  after ionization, assuming that the neutral cluster temperature  $T = 950 \text{ K}$ , ionization energy  $\text{IE} = 8 \text{ eV}$ , dissociation energy  $E_d = 6 \text{ eV}$ , and effective vibrational frequency  $k_0 = 10^{13} \text{ s}^{-1}$  [see the RRK formula (2)].

single variable for convenience; for the sake of brevity, we call this combined probability the “fragmentation probability.” Figure 5 shows these fragmentation probability distributions for  $(\text{ZrO}_2)_{10}$  clusters as a function of the number  $p$  of evaporated  $\text{ZrO}_2$  monomers plotted for the three ionization laser intensities  $I$ ,  $I \pm 3\sigma$ . The crossover point for the  $I \pm 3\sigma$  curves occurs at  $p = 2$  in Fig. 5. When the laser intensity increases from  $I - 3\sigma$  to  $I + 3\sigma$ , the probability to evaporate  $p = 0$  and 1  $\text{ZrO}_2$  monomers from cluster  $(\text{ZrO}_2)_{10}$

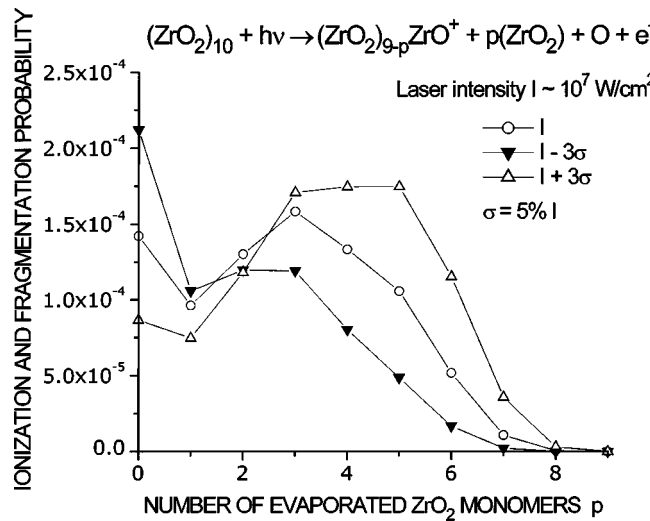


FIG. 5. The fragmentation probability distributions of  $(\text{ZrO}_2)_{10}$  clusters as functions of the number  $p$  of evaporated  $\text{ZrO}_2$  monomers calculated by formula (11) and plotted for ionization laser intensities  $I$ ,  $I - 3\sigma$ , and  $I + 3\sigma$ , with  $I \sim 10^7 \text{ W/cm}^2$  and  $\sigma = 5\% I$ . Notice the crossover between the  $I - 3\sigma$  and  $I + 3\sigma$  curves at  $p = 2$ . The values of parameters  $E_d$ ,  $E_{dl}$ ,  $\text{IE}$ ,  $x$ , and  $\sigma(1)It$  used in the simulation are the same as in Fig. 7.

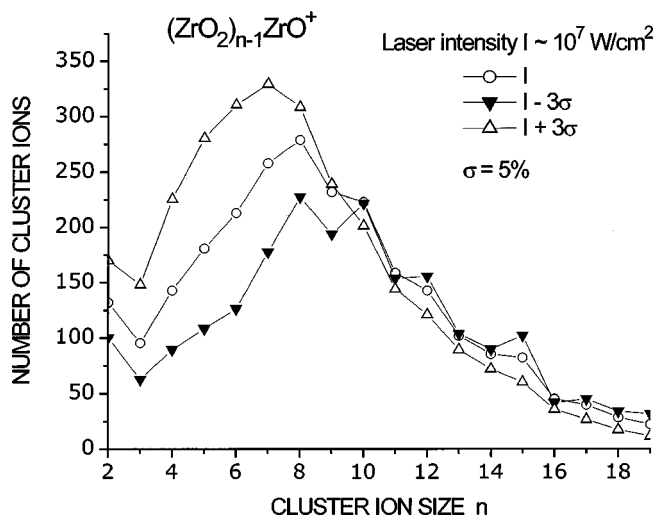


FIG. 6. The simulated  $(\text{ZrO}_2)_{n-1}\text{ZrO}^+$  mass spectra calculated from formulas (9) and (18) and plotted for ionization laser intensities  $I$ ,  $I - 3\sigma$ , and  $I + 3\sigma$ ,  $I \sim 10^7 \text{ W/cm}^2$  and  $\sigma = 5\%I$ . Notice the crossover between the  $I - 3\sigma$  and  $I + 3\sigma$  curves at  $n = 10$ . The values of parameters  $E_d$ ,  $E_{dl}$ , IE,  $x$ , and  $\sigma(1)It$  used in the simulation are the same as in Fig. 7.

decreases while the probability to evaporate  $p > 2$   $\text{ZrO}_2$  monomers from cluster  $(\text{ZrO}_2)_{10}$  increases. The  $(\text{ZrO}_2)_{9-p}\text{ZrO}^+$  ( $p > 2$ ) fragmentation products are formed at the expense of the  $(\text{ZrO}_2)_9\text{ZrO}^+$  parent cluster ions. [Note that in this model, loss of an oxygen atom in the final fragmentation and the corresponding change of cluster ion stoichiometry is also considered. This fragmentation step is in accordance with the measured mass spectrum as displayed in Fig. 3.] Thus, one would expect negative correlations between  $(\text{ZrO}_2)_{9-p}\text{ZrO}^+$  ( $p > 2$ ) and  $(\text{ZrO}_2)_9\text{ZrO}^+$  cluster ions.

Figure 6 shows the simulated  $(\text{ZrO}_2)_{n-1}\text{ZrO}^+$  mass spectra plotted for ionization laser intensities  $I - 3\sigma$ ,  $I$ , and

$I+3\sigma$ . When the laser intensity increases from  $I-3\sigma$  to  $I+3\sigma$ , the signal intensity for cluster size  $n > 10$  decreases while the signal intensity for cluster ions with cluster size  $n < 10$  increases. The  $(\text{ZrO}_2)_{n-1}\text{ZrO}^+$  ( $n < 10$ ) cluster ions are found at the expense of the  $(\text{ZrO}_2)_{n-1}\text{ZrO}^+$  ( $n > 10$ ) cluster ions. The simulated covariance matrix displayed in Table I thus shows negative correlations between  $(\text{ZrO}_2)_{9+p}\text{ZrO}^+$  and  $(\text{ZrO}_2)_{9-p}\text{ZrO}^+$  ( $p > 0$ ) cluster ions.

The above analysis and simulation for spectral covariances show that the cluster correlation behavior can be rationalized under the given experimental conditions and that the covariance matrix can be modeled. This process provides strong motivation for performing covariance mapping measurements of the experimental mass spectral data taken for a given laser pulse. Parent ion/fragment ion correlation patterns can thus be used as a probe of cluster ion fragmentation. In the remainder of this section, we present the experimental covariance maps as a function of laser intensity, and we present a model of cluster ion fragmentation dependent on a few parameters that are varied to fit both the measured spectral intensities and covariance matrices. This model will show how much to decrease the ionization laser intensity to suppress completely cluster ion fragmentation.

## **1. Experimental covariance matrices**

To analyze for correlations between signal intensities of any two mass spectral features  $x$  and  $y$  observed for a single ionization laser pulse, one records and stores each individual mass spectral scan  $i$  and calculates covariances  $C(x,y)$  from a set of up to  $n = 2500$  scans in the usual way,<sup>6</sup>

$$C(x,y) = \frac{1}{n} \sum_{i=1}^n (x_i - \bar{x})(y_i - \bar{y}) \quad (5)$$

in which

TABLE I. The simulated covariance matrix of  $(\text{ZrO}_2)_{n-1}\text{ZrO}^+$  cluster ions obtained for parameters  $T=950$  K,  $E_d=E_{dl}=6$  eV, IE=8 eV,  $x=1$ , and  $\sigma(1)It=0.83$ . This value for  $\sigma(1)It$  corresponds to photoabsorption cross section  $\sigma(1)\sim 10^{-17}$  cm $^2$  and ionization laser intensity  $I=10^7$  W/cm $^2$ . See text for explanation of the meaning of these parameters and how the covariance matrix has been calculated. To conserve space, all tabulated values have been multiplied by factor 1000. The leftmost column and the uppermost line in the table with numbers  $n$ ,  $2n-1$  indicate the cluster size  $n[n, 2n-1]\equiv(\text{ZrO}_2)_{n-1}\text{ZrO}^+$ .

TABLE II. The measured normalized covariance matrix for ionization laser intensity  $I=10^7 \text{ W/cm}^2$ . Normalized covariances are obtained from 2500 TOF mass spectral scans (each scan is recorded by a single laser pulse) using formula (7). The error bars have been obtained by recording 10 covariance matrices, each from 250 TOF mass spectral scans (the error bars are  $\pm 2\sigma$ ). To conserve space, all tabulated values have been multiplied by factor 1000. The leftmost column and the uppermost line in the table with numbers  $n$ ,  $2n-1 \equiv (\text{ZrO}_2)_{n-1}\text{ZrO}^+$ .

NC	2,3	3,5	4,7	5,9	6,11	7,13	8,15	9,17	10,19	11,21	12,23	13,25	14,27	15,29	16,31	17,33	18,35
1,1	$5 \pm 1$	$4 \pm 1$	$6 \pm 1$	$6 \pm 1$	$6 \pm 1$	$5 \pm 1$	$5 \pm 1$	$5 \pm 1$	$4 \pm 1$	$4 \pm 1$	$5 \pm 2$	$5 \pm 2$	$5 \pm 2$	$4 \pm 2$	$4 \pm 2$	$5 \pm 2$	
2,3		$8 \pm 1$	$7 \pm 1$	$6 \pm 1$	$4 \pm 1$	$2 \pm 0$	$1 \pm 1$	$0 \pm 1$	$-1 \pm 1$	$-2 \pm 1$	$-4 \pm 1$	$-5 \pm 1$	$-6 \pm 2$	$-7 \pm 2$	$-8 \pm 2$	$-8 \pm 2$	$-9 \pm 2$
3,5			$8 \pm 1$	$5 \pm 1$	$4 \pm 1$	$2 \pm 1$	$1 \pm 1$	$-1 \pm 1$	$-2 \pm 1$	$-3 \pm 1$	$-5 \pm 2$	$-6 \pm 2$	$-7 \pm 3$	$-9 \pm 2$	$-9 \pm 3$	$-10 \pm 3$	$-10 \pm 3$
4,7				$7 \pm 1$	$6 \pm 1$	$5 \pm 1$	$4 \pm 0$	$3 \pm 1$	$2 \pm 1$	$1 \pm 1$	$0 \pm 2$	$-1 \pm 2$	$-1 \pm 2$	$-2 \pm 1$	$-2 \pm 2$	$-2 \pm 2$	$-2 \pm 2$
5,9					$7 \pm 1$	$6 \pm 1$	$5 \pm 1$	$5 \pm 1$	$4 \pm 1$	$4 \pm 1$	$4 \pm 2$	$5 \pm 2$					
6,11						$7 \pm 1$	$6 \pm 1$	$6 \pm 1$	$6 \pm 1$	$7 \pm 2$	$7 \pm 2$	$8 \pm 2$	$9 \pm 2$				
7,13							$7 \pm 1$	$7 \pm 1$	$8 \pm 1$	$8 \pm 2$	$8 \pm 2$	$9 \pm 2$	$10 \pm 2$	$11 \pm 2$	$11 \pm 3$	$11 \pm 2$	$13 \pm 3$
8,15								$7 \pm 2$	$9 \pm 2$	$9 \pm 2$	$10 \pm 3$	$11 \pm 3$	$12 \pm 3$	$13 \pm 3$	$13 \pm 4$	$14 \pm 3$	$15 \pm 4$
9,17									$10 \pm 2$	$10 \pm 3$	$11 \pm 3$	$13 \pm 4$	$15 \pm 4$	$15 \pm 4$	$16 \pm 4$	$16 \pm 4$	$18 \pm 5$
10,19										$12 \pm 3$	$14 \pm 3$	$17 \pm 4$	$18 \pm 4$	$19 \pm 4$	$21 \pm 5$	$22 \pm 4$	$23 \pm 5$
11,21											$15 \pm 3$	$18 \pm 4$	$20 \pm 5$	$21 \pm 4$	$22 \pm 5$	$23 \pm 5$	$25 \pm 5$
12,23											$21 \pm 4$	$23 \pm 5$	$25 \pm 4$	$26 \pm 5$	$27 \pm 5$	$30 \pm 5$	
13,25												$27 \pm 6$	$29 \pm 6$	$31 \pm 7$	$32 \pm 7$	$35 \pm 7$	
14,27													$32 \pm 7$	$35 \pm 8$	$36 \pm 8$	$39 \pm 8$	
15,29														$38 \pm 7$	$39 \pm 7$	$43 \pm 7$	
16,31															$42 \pm 8$	$46 \pm 9$	
17,33																$47 \pm 9$	

$$\bar{x} = \frac{1}{n} \sum_{i=1}^n x_i, \quad \bar{y} = \frac{1}{n} \sum_{i=1}^n y_i \quad (6)$$

and  $x_i$ ,  $y_i$  are signal intensities (integrated over peak areas) of mass spectral peaks  $x$  and  $y$  in the single laser pulse scan  $i$ . Each single mass scan is thus recorded from a single ionization laser pulse and stored individually as a record in a computer. The covariance matrix is normalized by dividing each element of  $C(x,y)$  by the average signal intensity,

$$\bar{C}(x,y) = \frac{C(x,y)}{\bar{x}\bar{y}}. \quad (7)$$

This normalization scheme is chosen because normalized covariances  $\bar{C}(x,y)$  can be more easily simulated than the correlation coefficients,

$$\gamma(x,y) = \frac{C(x,y)}{[C(x,x)C(y,y)]^{1/2}}. \quad (8)$$

Tables II, III, and IV compare the measured normalized covariance matrices for ionization laser intensities  $I=1.1 \times 10^7 \text{ W/cm}^2$  (1 mJ/pulse),  $9.6 \times 10^6 \text{ W/cm}^2$  (0.86 mJ/pulse), and  $8.6 \times 10^6 \text{ W/cm}^2$  (0.77 mJ/pulse), respectively. Cluster ions with sizes  $n \geq n_t(I)$  negatively correlate with cluster ions with sizes  $n \leq 4$  for which  $n_t(I)$  is the laser intensity dependent threshold size for negative covariance. The value of  $n_t(I)$  increases with decreasing laser intensity, i.e.,  $n_t(I) = 10, 14$ , and  $17$  for laser energy 1, 0.86, and 0.77 mJ/pulse, respectively. No negative covariances are found for  $I < 0.71 \times 10^7 \text{ W/cm}^2$  ( $< 0.65 \text{ mJ/pulse}$ ). Disappearance of negative covariances with decreasing laser intensity indicates that

TABLE III. The measured normalized covariance matrix for ionization laser intensity  $I=0.8 \pm 10^7 \text{ W/cm}^2$ . Normalized covariances are obtained the same way as for Table II. To conserve space, all tabulated values have been multiplied by factor 1000. The leftmost column and the uppermost line in the table with numbers  $n$ ,  $2n-1 \equiv (\text{ZrO}_2)_{n-1}\text{ZrO}^+$ .

NC	2,3	3,5	4,7	5,9	6,11	7,13	8,15	9,17	10,19	11,21	12,23	13,25	14,27	15,29	16,31	17,33	18,35
1,1	$12 \pm 2$	$12 \pm 2$	$14 \pm 3$	$14 \pm 3$	$14 \pm 3$	$12 \pm 3$	$11 \pm 2$	$10 \pm 2$	$9 \pm 3$	$8 \pm 3$	$8 \pm 2$	$8 \pm 2$	$7 \pm 2$	$6 \pm 2$	$6 \pm 2$	$5 \pm 1$	$6 \pm 1$
2,3		$18 \pm 2$	$16 \pm 2$	$14 \pm 2$	$12 \pm 2$	$11 \pm 2$	$8 \pm 2$	$6 \pm 2$	$4 \pm 2$	$3 \pm 2$	$1 \pm 2$	$0 \pm 2$	$-2 \pm 2$	$-4 \pm 2$	$-4 \pm 2$	$-5 \pm 2$	$-5 \pm 1$
3,5			$17 \pm 3$	$15 \pm 1$	$13 \pm 2$	$10 \pm 2$	$8 \pm 2$	$6 \pm 1$	$4 \pm 1$	$2 \pm 1$	$0 \pm 2$	$-1 \pm 1$	$-3 \pm 2$	$-5 \pm 2$	$-6 \pm 2$	$-7 \pm 2$	$-7 \pm 2$
4,7				$15 \pm 2$	$13 \pm 3$	$12 \pm 2$	$9 \pm 2$	$8 \pm 2$	$6 \pm 2$	$5 \pm 2$	$3 \pm 1$	$2 \pm 1$	$1 \pm 1$	$-1 \pm 1$	$-1 \pm 1$	$-3 \pm 0$	$-3 \pm 1$
5,9					$14 \pm 2$	$12 \pm 2$	$10 \pm 2$	$9 \pm 2$	$8 \pm 2$	$7 \pm 2$	$5 \pm 2$	$5 \pm 2$	$4 \pm 2$	$3 \pm 2$	$3 \pm 2$	$2 \pm 2$	$2 \pm 1$
6,11						$12 \pm 3$	$10 \pm 2$	$9 \pm 2$	$9 \pm 2$	$8 \pm 2$	$7 \pm 2$	$8 \pm 2$	$7 \pm 2$	$6 \pm 2$	$6 \pm 2$	$5 \pm 2$	$5 \pm 1$
7,13							$9 \pm 2$	$9 \pm 2$	$8 \pm 2$	$8 \pm 2$	$7 \pm 2$	$7 \pm 2$	$6 \pm 2$	$6 \pm 2$	$6 \pm 2$	$5 \pm 2$	$5 \pm 1$
8,15								$8 \pm 2$	$8 \pm 2$	$7 \pm 2$	$7 \pm 2$	$7 \pm 2$	$7 \pm 2$	$7 \pm 2$	$7 \pm 2$	$6 \pm 1$	$7 \pm 1$
9,17									$8 \pm 2$	$8 \pm 2$	$8 \pm 2$	$9 \pm 2$	$8 \pm 2$	$9 \pm 2$	$9 \pm 2$	$8 \pm 2$	$9 \pm 2$
10,19									$9 \pm 3$	$9 \pm 2$	$11 \pm 3$	$11 \pm 3$	$11 \pm 3$	$11 \pm 2$	$11 \pm 2$	$12 \pm 2$	
11,21										$10 \pm 3$	$11 \pm 3$	$12 \pm 4$	$12 \pm 3$	$12 \pm 3$	$13 \pm 4$	$13 \pm 3$	
12,23											$12 \pm 3$	$13 \pm 3$	$14 \pm 3$	$14 \pm 3$	$15 \pm 3$	$16 \pm 3$	
13,25												$16 \pm 4$	$16 \pm 4$	$17 \pm 3$	$18 \pm 3$	$19 \pm 4$	
14,27													$18 \pm 4$	$19 \pm 4$	$20 \pm 4$	$21 \pm 5$	
15,29													$20 \pm 4$	$21 \pm 4$	$23 \pm 5$		
16,31														$23 \pm 4$	$24 \pm 4$		
17,33															$26 \pm 6$		

TABLE IV. The measured normalized covariance matrix for ionization laser intensity  $I=0.75 \times 10^7 \text{ W/cm}^2$ . Normalized covariances are obtained the same way as for Table II. To conserve space, all tabulated values have been multiplied by factor 1000. The leftmost column and the uppermost line in the table with numbers  $n$ ,  $2n-1$  indicate the cluster size  $n$  [ $n, 2n-1 \equiv (\text{ZrO}_2)_{n-1}\text{ZrO}^+$ ].

NC	2,3	3,5	4,7	5,9	6,11	7,13	8,15	9,17	10,19	11,21	12,23	13,25	14,27	15,29	16,31	17,33	18,35
1,1	$17 \pm 1$	$18 \pm 3$	$20 \pm 3$	$21 \pm 1$	$19 \pm 1$	$18 \pm 2$	$17 \pm 2$	$15 \pm 1$	$16 \pm 2$	$14 \pm 1$	$13 \pm 2$	$14 \pm 3$	$13 \pm 3$	$12 \pm 4$	$11 \pm 4$	$10 \pm 4$	$10 \pm 6$
2,3		$17 \pm 3$	$17 \pm 3$	$17 \pm 2$	$15 \pm 1$	$13 \pm 2$	$11 \pm 2$	$9 \pm 1$	$7 \pm 2$	$5 \pm 1$	$4 \pm 1$	$3 \pm 2$	$2 \pm 2$	$0 \pm 1$	$-1 \pm 2$	$-2 \pm 2$	$-3 \pm 4$
3,5			$19 \pm 4$	$19 \pm 2$	$15 \pm 3$	$13 \pm 3$	$11 \pm 3$	$10 \pm 2$	$8 \pm 2$	$5 \pm 2$	$4 \pm 2$	$3 \pm 4$	$3 \pm 3$	$1 \pm 2$	$0 \pm 3$	$-2 \pm 3$	$-2 \pm 4$
4,7				$20 \pm 3$	$17 \pm 3$	$16 \pm 4$	$14 \pm 3$	$12 \pm 2$	$11 \pm 2$	$9 \pm 2$	$7 \pm 2$	$8 \pm 2$	$6 \pm 2$	$5 \pm 2$	$4 \pm 3$	$2 \pm 3$	$3 \pm 4$
5,9					$19 \pm 1$	$17 \pm 2$	$15 \pm 1$	$14 \pm 1$	$13 \pm 1$	$11 \pm 1$	$11 \pm 1$	$11 \pm 2$	$10 \pm 3$	$9 \pm 3$	$7 \pm 4$	$7 \pm 4$	$7 \pm 5$
6,11						$16 \pm 2$	$15 \pm 1$	$14 \pm 1$	$14 \pm 1$	$13 \pm 1$	$13 \pm 2$	$13 \pm 2$	$12 \pm 3$	$11 \pm 3$	$10 \pm 2$	$10 \pm 4$	
7,13							$15 \pm 2$	$14 \pm 1$	$14 \pm 1$	$13 \pm 1$	$13 \pm 1$	$14 \pm 1$	$13 \pm 2$	$12 \pm 2$	$12 \pm 2$	$12 \pm 3$	
8,15								$14 \pm 2$	$15 \pm 2$	$14 \pm 1$	$14 \pm 2$	$16 \pm 2$	$15 \pm 3$	$15 \pm 3$	$14 \pm 3$	$14 \pm 3$	$14 \pm 4$
9,17									$15 \pm 1$	$15 \pm 1$	$15 \pm 2$	$17 \pm 2$	$17 \pm 3$	$17 \pm 2$	$17 \pm 2$	$17 \pm 2$	$17 \pm 3$
10,19										$17 \pm 1$	$19 \pm 1$	$21 \pm 2$	$21 \pm 2$	$22 \pm 2$	$22 \pm 2$	$22 \pm 2$	$24 \pm 3$
11,21											$19 \pm 2$	$22 \pm 2$	$22 \pm 3$	$24 \pm 3$	$23 \pm 2$	$23 \pm 2$	$25 \pm 4$
12,23												$25 \pm 3$	$25 \pm 3$	$27 \pm 3$	$27 \pm 2$	$27 \pm 2$	$29 \pm 5$
13,25													$29 \pm 4$	$31 \pm 3$	$32 \pm 4$	$32 \pm 4$	$35 \pm 5$
14,27														$32 \pm 3$	$33 \pm 4$	$34 \pm 3$	$37 \pm 6$
15,29															$36 \pm 2$	$37 \pm 2$	$39 \pm 5$
16,31															$39 \pm 3$	$41 \pm 5$	
17,33																$43 \pm 5$	

they are caused by cluster ion fragmentation; fragmentation decreases as laser intensity is decreased and thus, negative covariances also become smaller and eventually disappear. This is in contrast to cluster growth dominated covariances; their pattern does not change with changing laser intensity.<sup>6</sup>

Additional evidence that the experimental negative covariances in these data sets are fragmentation related comes from the following observation. Instead of integrating the  $x_i$ ,  $y_i$  signal intensities for use in Eq. (5) over the entire mass peak, the peak can be divided in half; an early time ("left") half, and a late time ("right") half. This yields four different covariance values for the peaks  $x$  and  $y$ , correlating left-left, right-right, left-right, and right-left components. For cluster sizes  $m > n$ , the highest negative normalized covariance occurs between the left half of the mass peak at cluster size  $m$  and the right half of the mass peak at cluster size  $n$ . The smallest negative covariance is found between the right half of the mass peak at cluster size  $m$  and the left half of mass peak at cluster size  $n$ . This observation of partial peak covariances is consistent with the idea that the parent ion intensity is mostly concentrated in the center and left half (early times) of the mass peak, whereas the fragment ion intensity is mostly concentrated in the right half (and right tail-late times) of the mass peak. This detailed inhomogeneous distribution of the ion kinetic energies arises because the kinetic energy of the ions formed by fragmentation in the ion source of the time-of-flight mass spectrometer is slightly less than the kinetic energy of the parent ions due to the time required for the fragmentation process. This effect is most pronounced at very high laser intensities ( $I > 1 \times 10^7 \text{ W/cm}^2, 1 \text{ mJ/pulse}$ ).

## 2. Modeling covariance matrices

Details of the cluster ion fragmentation process can be elucidated through modeling of the measured normalized covariance matrices (Tables II, III, and IV). The ionization la-

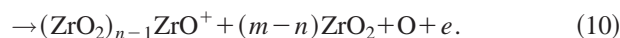
ser intensity dependent cluster ion distribution  $J(n)$  is related to the neutral cluster distribution  $N(m)$  by the linear transformation,

$$J(n) = \sum_{m=n}^{m_{\text{MAX}}} FPM(n,m)N(m). \quad (9)$$

$J(n)$  expresses the  $(\text{ZrO}_2)_n^+$  or  $(\text{ZrO}_2)_{n-1}\text{ZrO}^+$  cluster ion signal intensity as a function of cluster size  $n$ .  $m_{\text{MAX}}$  is the maximum neutral cluster size considered ( $m_{\text{MAX}}=25$ ) and  $FPM(n,m)$  is the fragmentation and ionization probability matrix that gives the probability for the reaction



or



$FPM(n,m)=0$  for  $n > m$ . The matrix  $FPM$  is expressed in the form,

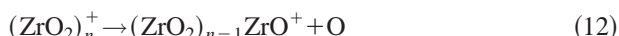
$$FPM(n,m) = \sum_{j=j_{\text{MIN}}}^{j_{\text{MAX}}} FAM(m,m-n,j)AP(j). \quad (11)$$

$j$  is the number of absorbed photon,  $j_{\text{MIN}}=2$  is the minimum number of absorbed photons needed for ionization,  $j_{\text{MAX}}$  is the maximum number of absorbed photons considered ( $j_{\text{MAX}}=25$  in this work),  $FAM(m,p,j)$  is the probability to evaporate  $p$   $\text{ZrO}_2$  molecules from the cluster ion  $(\text{ZrO}_2)_m^+$  or  $(\text{ZrO}_2)_{m-1}\text{ZrO}^+$  with internal energy corresponding to absorption of  $j$  photons, and  $AP(j)$  is the probability that the  $(\text{ZrO}_2)_m$  neutral cluster absorbs exactly  $j$  photons and will be ionized.

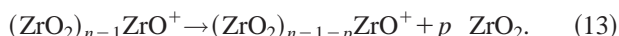
The matrix elements  $FAM(m,p,j)$  are calculated by solving a system of differential equations for sequential evaporation of  $p$   $\text{ZrO}_2$  molecules with fragmentation rate constants calculated from the RRK formula given in Eq. (2). This approach introduces three parameters into the model: the effective vibrational frequency for the reaction coordi-

nate  $k_0$ , the activation energy for the  $\text{ZrO}_2$  evaporation  $E_d$ , and the cluster ionization energy IE. The total energy deposited in a cluster [to be used in Eq. (2)] is  $E=jh\nu-\text{IE}$ , assuming that little energy is carried away by the ejected electron. Parameters  $k_0$ ,  $E_d$ , and IE are cluster size dependent. Use of a more sophisticated method for estimation of the rate constant for dissociation would have questionable value for accuracy of the model, since cluster dissociation energies  $E_a$  are not known, and the characteristics of the transition state (and other parameters introduced below) vary with cluster size.

At high ionization laser intensities, the loss of an oxygen atom is also considered (in accordance with the mass spectrum shown in Fig. 3). The fragmentation step



can be added to the simulation, and is characterized by an activation energy  $E_{dl}$ . This fragmentation occurs prior to the  $\text{ZrO}_2$  evaporation sequence,



The activation energy  $E_{dl}$  is the fourth parameter of the model ( $E_{dl}$  is assumed to be cluster size independent for simplicity). The parent ion intensity is then the sum of the calculated  $(\text{ZrO}_2)_{n-1}\text{ZrO}^+$  and  $(\text{ZrO}_2)_n^+$  intensities and the fragment ion intensities are the calculated  $(\text{ZrO}_2)_{n-1-p}\text{ZrO}^+$  ( $p > 0$ ) intensities. Fragmentation step Eq. (12) is not considered for low laser intensities. This procedure follows the experimental results, and it actually increases the fragmentation probabilities at low laser intensities compared to those at higher laser intensities. Since we are looking for the upper bound of the fragmentation probabilities at low laser intensity, this rather crude procedure is an acceptable approach to the estimate of cluster ion fragmentation as a function of laser intensity.

The photoabsorption and ionization probability matrix  $AP(j)$  is calculated with these assumptions: (1) the cluster must absorb at least  $j_{\text{MIN}}=2$  photons to be ionized (Fig. 2); and (2) absorption of the first photon populates an excited electronic state that has a lifetime  $\tau$  due to internal conversion. Under these assumption, matrix elements  $AP(j)$  are expressed in the form,

$$AP(j) = \frac{\tau}{t} (\sigma It)^2 \frac{(\sigma It)^{j-2}}{(j-1)!} \exp(-\sigma It) \quad (14)$$

in which  $j$  is the number of absorbed photons ( $j \geq j_{\text{MIN}} = 2$ ),  $t$  is the time duration of the ionization laser pulse ( $t \sim 10 \text{ ns}$ ),  $\sigma$  is the photoabsorption cross section, and  $I$  is the ionization laser intensity (in photons/cm<sup>2</sup>/s).

For simplicity, the lifetime  $\tau$  is assumed to be cluster size independent under this assumption, the ratio  $\tau/t$  affects the total ionization efficiency of clusters, but not the cluster fragmentation probabilities. The ratio  $\tau/t$  only affects the scale of the ordinate in Figs. 4–8. The choice of this parameter is thus completely arbitrary. We take  $\tau/t=10^{-4}$ , corresponding to  $\tau \sim 1 \text{ ps}$ . This gives a reasonable ratio for the number of cluster ions and the number of neutral clusters, which corresponds to the measured cluster ion signal inten-

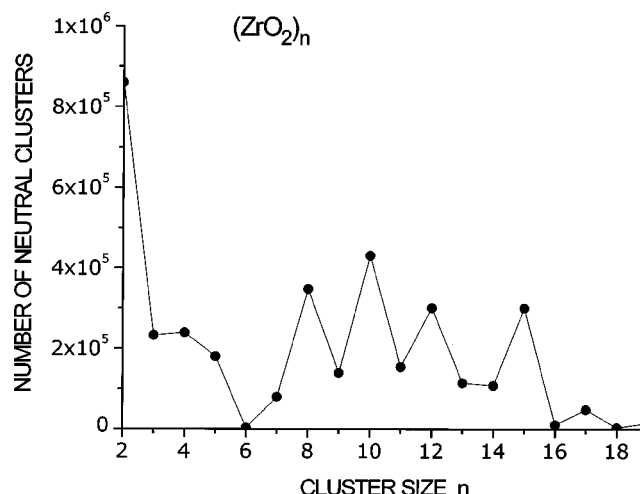


FIG. 7. Simulated neutral cluster distribution, calculated from the ion distribution shown in Fig. 3 by formula (18) using parameter values  $E_d=E_{dl}=6 \text{ eV}$ ,  $\text{IE}=8 \text{ eV}$ ,  $x=1$ , and  $\sigma(1)It=0.83$ . The value of  $\sigma(1)It$  taken corresponds to a photoabsorption cross section  $\sigma(1) \sim 10^{-17} \text{ cm}^2$ .

sities and the estimated neutral cluster concentrations in the molecular beam. Based on Eq. (14), the total ionization probability can be expressed as

$$\sum_{j=2}^{\infty} AP(j) = \frac{\tau}{t} (\sigma It) [1 - \exp(-\sigma It)]. \quad (15)$$

The photoabsorption cross section  $\sigma$  increases with cluster size  $n$  according to the relation

$$\sigma(n) = \sigma(1)n^x \quad (16)$$

in which  $\sigma(1)$  is the photoabsorption cross section for cluster size 1 ( $\text{ZrO}_2$ ). The exponent  $x$  and the product  $\sigma(1)It$  are the fifth and sixth parameters of the model [i.e.,  $k_0$ ,  $E_d$ , IE,  $E_{dl}$ ,  $x$ ,  $\sigma(1)It$ ].

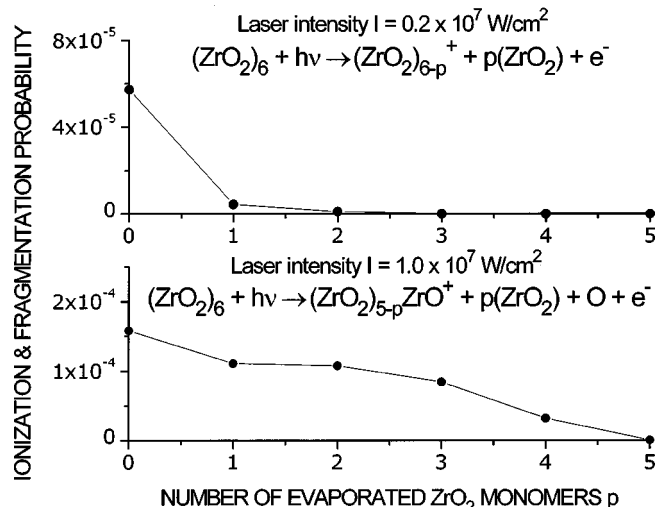


FIG. 8. The simulated fragmentation probability distributions of  $(\text{ZrO}_2)_6$  compared for two different values of the  $\sigma(1)It$  parameter corresponding to ionization laser intensities  $I \sim 1$  and  $0.2 \times 10^7 \text{ W/cm}^2$ , respectively (the values of parameters  $E_d$ ,  $E_{dl}$ , IE, and  $x$  are the same as in Fig. 7). Notice the significant drop of fragmentation probability upon decreasing the laser intensity.

The photoabsorption probability distribution of Eq. (14) differs slightly from the Poisson distribution,

$$AP(j) = \frac{\tau}{t} (\sigma It)^2 \frac{(\sigma It)^{j-2}}{(j-2)!} \exp(-\sigma It). \quad (17)$$

Equations (14) and (17) describe two slightly different ionization models. They treat differently the case for which the electronic state populated by absorption of the first photon undergoes internal conversion to the vibrational modes of the ground electronic state at equal energy. In the model corresponding to the Poisson photoabsorption distribution Eq. (17), clusters that undergo internal conversion can be re-excited by absorbing another photon with the same photoabsorption cross section. This process yields cycling between the ground and excited electronic states of the neutral cluster. On the other hand, the model corresponding to the photoabsorption distribution depicted in Eq. (14) assumes clusters that undergo internal conversion cannot be ionized either because their re-excitation cross section is small or, more likely, because the lifetime of the excited state becomes much shorter following vibrational excitation resulting from the internal conversion. In this latter model of Eq. (14), the absorption of all but two photons occurs in the ion.

Using the Poisson photoabsorption distribution Eq. (17), the measured covariance matrix could not be fit by any combination of the six parameters mentioned above [i.e.,  $k_0$ ,  $E_d$ , IE,  $E_{dl}$ ,  $x$ ,  $\sigma(1)It$ ]. The following problem arises for this model: either the simulated threshold size for negative correlation is much higher than the experimental value, or the simulated neutral cluster distribution has negative cluster intensities for small neutral cluster sizes (i.e., the simulated fragmentation of larger clusters yields many more cluster ions with small cluster sizes than are observed experimentally). Under the constraint of nonnegative neutral cluster intensities, the smallest threshold size for negative correlations is  $n_t=17$ , far larger than the experimentally observed  $n_t=10$ .

Employing photoabsorption distribution Eq. (14), however, many combinations of the six model fitting parameters give very good agreement between the measured and simulated covariance matrices. The model is too simple and approximate to draw any firm conclusions about ionization dynamics based on this information, but perhaps the re-excitation cross section for the neutral does decrease or the lifetime  $\tau$  of the intermediate electronic state of the neutral becomes much shorter after vibrational excitation resulting from internal conversion.

Modeling of the measured mass spectra and the normalized covariance matrices is accomplished in two steps. In the first step, the neutral cluster distribution  $N(m)$  is calculated from the cluster ion distribution  $J(n)$  measured at high ionization laser intensity ( $I \sim 1 \times 10^7 \text{ W/cm}^2$ , see Fig. 3) using

$$N(m) = \sum_{n=1}^m FPM^{-1}(m,n)J(n), \quad (18)$$

in which  $FPM^{-1}$  is the inverse matrix of  $FPM$  [Eq. (11)]. The neutral distribution  $N(m)$  so obtained is a function of the six parameters of the model,  $k_0$ ,  $E_d$ , IE,  $E_{dl}$ ,  $x$ , and

$\sigma(1)It$ . These six parameters are used to calculate  $FPM$ .  $k_0$  is kept fixed at  $10^{13} \text{ s}^{-1}$ . This is a reasonable choice for the effective vibrational frequency, as the  $(\text{ZrO}_2)_6$  modes (see below) range from  $86$  to  $903 \text{ cm}^{-1}$ . Parameters  $E_d$  and  $E_{dl}$  are varied between  $4.35$  and  $6.5 \text{ eV}$ . This interval is chosen based on *ab initio* calculational results for adiabatic dissociation energies of  $(\text{ZrO}_2)_n$ ,  $n=4,5,6$ , neutral clusters. The adiabatic dissociation energies for clusters  $n=4,5,6$  are, respectively,  $5.65$ ,  $6.10$ , and  $4.35 \text{ eV}$ . The ionization energy IE is varied between  $7$  and  $8.5 \text{ eV}$ . This interval is chosen based on both experiment (IE >  $6.43 \text{ eV}$ ) and *ab initio* calculations. The calculated adiabatic ionization energies of  $(\text{ZrO}_2)_n$ ,  $n=4,5,6$ , clusters are  $7.6$ ,  $7.7$ , and  $8.5 \text{ eV}$ , respectively. The parameter  $x$  is varied between  $0.66$  and  $1.0$ . For  $x=0.66$ , the photoabsorption cross section scales with the geometric cross section of the cluster. For  $x=1$ , the photoabsorption cross section scales with the cluster volume.<sup>4(b)</sup>

The neutral cluster distribution is calculated for many different combinations of parameters  $E_d$ , IE,  $E_{dl}$ , and  $x$ , taken from the intervals given above in the previous paragraph. For each combination of parameters  $E_d$ , IE,  $E_{dl}$ , and  $x$ , the remaining parameter  $\sigma(1)It$  is varied until the threshold cluster size  $n_t$  for a negative covariance matrix element matches the threshold cluster size  $n_t=10$  in the measured covariance matrix. Varying parameter  $\sigma(1)It$  for a given ionization laser intensity  $I$  corresponds to fitting the unknown photoabsorption cross section  $\sigma(1)$  to the experimental data. Parameter  $\sigma(1)It$  determines how many photons are absorbed by the cluster, and thus, the extent of fragmentation: the higher the value of  $\sigma(1)I$ , the more cluster fragmentation and the lower the simulated threshold cluster size  $n_t$ .

The second step of this simulation program is to obtain the covariance matrix that matches the calculated cluster ion and neutral cluster distributions. The covariance matrix (needed to obtain the threshold cluster size  $n_t$  for negative covariances) is calculated by the following procedure. Once the neutral cluster distribution  $N(m)$  is calculated, a vector of 2500 different values of  $\sigma(1)I^*t$  is generated for which  $\sigma(1)I^*t$  is taken randomly from a normal (Gaussian) distribution with mean equal to  $\sigma(1)It$  and variance equal to  $[5\% \sigma(1)It]^2$ .  $5\%$  is the standard deviation of the laser intensity distribution for the ionization laser. This simulates pulse-to-pulse fluctuations of the ionization laser intensity  $I$ . Cluster ion distribution  $J^*(n)$  is calculated for each value of  $\sigma(1)I^*t$  from Eq. (9). The normalized covariance matrix is calculated from a set of 2500 so obtained distributions  $J^*(n)$  using Eqs. (5)–(7).

Figure 7 shows a typical simulated neutral cluster distribution, calculated from the ion distribution shown in Fig. 3 using parameter values  $E_d=E_{dl}=6 \text{ eV}$ , IE =  $8 \text{ eV}$ ,  $x=1$ , and  $\sigma(1)It=0.83$  [corresponding to a photoabsorption cross section of  $\sigma(1) \sim 10^{-17} \text{ cm}^{-2}$ ]. The local intensity fluctuations in the distribution (the “magic numbers”) do not exactly reproduce the measured mass spectrum shown in Fig. 1, because in this simple model cluster, dissociation energies are assumed to be independent of cluster size  $n$ . *Ab initio* calculations presented in the next section show that this assumption is unjustified and some cluster sizes are more stable than

others; naturally,  $(\text{ZrO}_2)_5$  is more stable than  $(\text{ZrO}_2)_4$  and  $(\text{ZrO}_2)_6$ , consistent with the magic number at cluster size  $n = 5$  in the measured mass spectra of Fig. 1. This cluster size ( $n = 5$ ) is not "magic" in the simulated neutral distribution because in the present model, the assumption is made, to a first approximation, that the  $E_d[(\text{ZrO}_2)_{4,5,6}]$  are all equal. The neutral distribution shown in Fig. 7 is only a first order approximation to be used to get a general idea about the overall trend in cluster size dependant neutral cluster intensities, not the "magic numbers."

The corresponding simulated covariance matrix for the distribution of Fig. 7 is shown in Table I. The measured covariance matrix is presented in Table II. The measured and simulated threshold size  $n_t$  for negative covariances are in good agreement.

One of the goals of these simulations is to determine the laser intensity for which cluster ion fragmentation does not dominate the mass spectrum of the clusters, and can be ignored as a small effect. At this laser intensity, the measured cluster ion distribution observed in the mass spectrum would reliably reflect the true neutral cluster distribution. Thus, in the second step of this simulation program, the value of the parameter  $\sigma(1)It$  is progressively decreased and the total fragmentation probability  $N_f/N_p(n)$  is calculated for each cluster size  $n$ , in which  $N_p(n) = FPM(n,n)$  is the  $(\text{ZrO}_2)_n^+$  parent ion intensity and  $N_f = \sum_{p=1}^{n-1} FPM(n-p,n)$  is the sum of fragment ion intensities taken over all fragment ions  $(\text{ZrO}_2)_{n-p}^+$  ( $p > 0$ ). The value of parameter  $\sigma(1)It$  is decreased until the total fragmentation probability  $N_f/N_p(n)$  falls below a specified limit.

The main objective of this simulation effort is to discern whether the  $(\text{ZrO}_2)_5^+$  ion is "magic" in the mass spectrum of  $(\text{ZrO}_2)_n^+$  because of exceptional stability of the  $(\text{ZrO}_2)_5$  neutral cluster or because of the fragmentation of large cluster ions feeding the stable  $(\text{ZrO}_2)_5^+$  ion. In Fig. 1, the  $(\text{ZrO}_2)_5^+$  cluster ion intensity is more than 250% larger than the  $(\text{ZrO}_2)_6^+$  cluster ion intensity and more than 150% of the sum of  $(\text{ZrO}_2)_6^+$  and  $(\text{ZrO}_2)_6\text{O}^+$  cluster ion intensities. Such an intensity increase of  $(\text{ZrO}_2)_5^+$  compared to that of  $(\text{ZrO}_2)_6^+$  could be caused by fragmentation only if the fragmentation probability  $N_f/N_p(6)$  is higher than 50% [assuming that both  $(\text{ZrO}_2)_6^+$  and  $(\text{ZrO}_2)_6\text{O}^+$  fragment to  $(\text{ZrO}_2)_5^+$ ].

TABLE V. Total fragmentation probabilities  $N_f/N_p$  shown for different combinations of parameters  $E_d$ ,  $E_{dl}$ , IE, and  $x$ . The  $\sigma(1)It$  parameter is decreased to 20% of the  $\sigma(1)It$  value that fits the measured covariance matrix. This is done to simulate fragmentation at 20% laser intensity ( $0.2 \times 10^7 \text{ W/cm}^2$ , see text for details). The calculated ionization cross sections  $\sigma$  are also shown.

$E_d$ (eV)	$E_{dl}$ (eV)	$x = 0.6666$		$x = 1.0$	
		IE=7 eV	IE=8 eV	IE=7 eV	IE=8 eV
4.35	4.35	$\sigma(10^{-17} \text{ cm}^2)$	1.54	1.73	0.81
		$N_f/N_p (\%)$	26.8	17.9	25.8
5	4	$\sigma(10^{-17} \text{ cm}^2)$	1.87	1.83	0.95
		$N_f/N_p (\%)$	13.7	11.7	12.2
5	5	$\sigma(10^{-17} \text{ cm}^2)$	1.83	1.82	0.97
		$N_f/N_p (\%)$	13.2	11.6	12.4
6	5	$\sigma(10^{-17} \text{ cm}^2)$	2.10	2.12	1.04
		$N_f/N_p (\%)$	13.3	10.3	11.1
6	6	$\sigma(10^{-17} \text{ cm}^2)$	2.12	2.14	1.04
		$N_f/N_p (\%)$	13.4	10.5	11.1

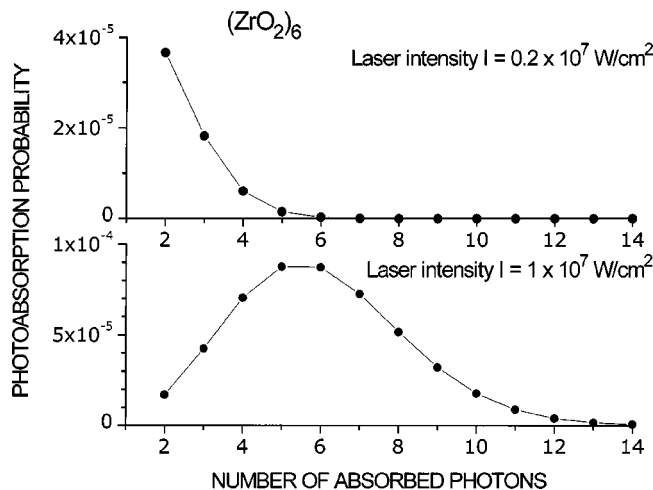


FIG. 9. Photoabsorption probability distributions of  $(\text{ZrO}_2)_6$  compared for two different values of the  $\sigma(1)It$  parameter corresponding to ionization laser intensities  $I \sim 1$  and  $0.2 \times 10^7 \text{ W/cm}^2$ , respectively.

The purpose of the simulation is to determine whether or not the mass spectra of Fig. 1 are recorded at sufficiently low ionization laser intensity that the fragmentation probability for cluster  $n = 6$  to  $n = 5$  is far below 50%. Therefore, in the simulation, the upper limit for fragmentation  $N_f/N_p(6) \sim 25\%$  is chosen.

The neutral cluster distribution obtained in the first step of the simulation procedure is kept fixed and the cluster ion distribution, the covariance matrix, and the fragmentation probability distributions are recalculated for each new value of parameter  $\sigma(1)It$ . Figure 8 shows how the fragmentation probability distribution changes as  $\sigma(1)It$  is decreased to 20% of its original value, with the other parameters held fixed as indicated above. The total fragmentation probability, under these simulation conditions, decreases to 8.6%, which is a negligible value. Figure 9 displays the corresponding change in the photoabsorption probability distribution. The decrease of the parameter  $\sigma(1)It$  in the simulation models the decrease of the ionization laser intensity in the experiment.

Table V presents the total fragmentation probabilities for different combination of parameters  $E_d$ ,  $E_{dl}$ , IE, and  $x$  for

TABLE VI. Calculated dipole moment, Zr–O bond distance, and O–Zr–O bond angle for the  $\text{ZrO}_2$  molecule obtained on different theory levels (see the text for details). The experimental values from Ref. 15 are also shown for comparison.

Method	Basis set	...	STO3G	3-21G	3-21G+	LANL2DZ	LANL2DZ+
Experiment	$r$ ( $\text{\AA}$ )	1.771					
	$\alpha$ ( $^\circ$ )	108.1					
	$\mu$ (D)	7.8					
RHF	$r$ ( $\text{\AA}$ )		1.760	1.754	1.776	1.788	1.786
	$\alpha$ ( $^\circ$ )		103.5	107.2	110.8	111.7	111.8
	$\mu$ (D)		6.5	8.5	9.4	9.6	9.6
BPW91	$r$ ( $\text{\AA}$ )	1.799	1.783	1.804	1.813	1.814	
	$\alpha$ ( $^\circ$ )	100.0	102.5	105.8	106.1	106.1	
	$\mu$ (D)	4.5	6.6	7.7	7.6	7.8	
B3LYP	$r$ ( $\text{\AA}$ )	1.789	1.775	1.797	1.806	1.807	
	$\alpha$ ( $^\circ$ )	100.6	103.0	106.7	107.2	107.2	
	$\mu$ (D)	5.0	7.0	8.2	8.0	8.2	

$\sigma(1)It$  decreased to 20% of the  $\sigma(1)It$  value that fits the measured covariance matrix ( $k_0$  is fixed as  $10^{13} \text{ s}^{-1}$ ). The maximum total fragmentation probability taken over all the parameter combinations is  $\sim 25\%$ . We conclude that decreasing the ionization laser intensity to  $\sim 20\%$  of  $10^7 \text{ W/cm}^2$  ( $\sim 1 \text{ mJ/pulse}$ ) or about  $200 \mu\text{J}/\text{pulse}$  laser energy for the present experimental conditions will yield less than the desired upper limit for  $N_f/N_p(6)$ .

These data analysis methods and simulation of the measured mass spectra and concomitant covariance matrices reveal that, at the ionization laser intensity employed to record the mass spectra shown in Fig. 1, cluster ion fragmentation is too small to cause the observed enhancement of the  $(\text{ZrO}_2)_5^+$  ion intensity. The  $(\text{ZrO}_2)_5^+$  cluster is intense in the mass spectrum of zirconium oxide clusters (i.e., a “magic number”  $n=5$ ) because of exceptional stability of the  $(\text{ZrO}_2)_5$  neutral cluster, not because of the exceptional stability of the  $(\text{ZrO}_2)_5^+$  cluster ion. This conclusion is reached based on a semiquantitative analysis of the measured fragmentation induced covariance matrix under experimental conditions for which the number of photons absorbed by the cluster varies on a pulse-to-pulse basis due to ionization laser intensity fluctuations. Additionally, the simulation leads to the conclusion that neutral clusters absorb two photons to ionize, and that subsequent photoabsorption, which leads to cluster fragmentation, occurs for the ionized clusters at high ionization laser intensity.

#### IV. CALCULATION OF $(\text{ZrO}_2)_n$ CLUSTER STRUCTURES AND ENERGIES

To reveal the origin of the  $(\text{ZrO}_2)_5$  neutral cluster special stability and to learn the structural trends in the zirconium oxide neutral cluster distribution,  $(\text{ZrO}_2)_n$  cluster structures are calculated employing density functional theory (DFT) and the *ab initio* Hartree–Fock method as implemented in GAUSSIAN 98 (Ref. 10) and CERIUS 3.8 programs.<sup>11</sup> As an internal check on the quality of these rather low level calculations, a number of different approaches is taken to arrive at these results, as will be presented below.

The DFT gradient corrected correlation functional (Perdew and Wang<sup>12</sup>) and the gradient corrected exchange functional (Becke<sup>13</sup>) are employed with the GAUSSIAN 98 program

(BPW91). Los Alamos effective core potentials [LANL2DZ (Ref. 14)] are used to reduce the number of explicitly treated electrons for each zirconium atom to four valence electrons ( $5s^24d^2$ ) and light eight outer shell core electrons ( $4s^24p^6$ ). Effective core potentials are not used for oxygen atoms—all eight electrons for each oxygen atom are treated explicitly. The LANL2 effective core potentials come with two basis set versions. The valence double zeta basis set LANL2DZ is used for zirconium atoms and the D95 full double-zeta basis set [Dunning’s contraction of Huzinaga’s ( $9s,5p$ ) basis to [ $4s,2p$ ]] is employed for oxygen atoms throughout these calculations.<sup>10</sup> This level of theory gives rather good agreement with the measured dipole moment and rotational constants of the  $\text{ZrO}_2$  molecule.<sup>15</sup>

Table VI presents the dipole moment, Zr–O bond distance, and O–Zr–O bond angle for the  $\text{ZrO}_2$  molecule obtained by different theory levels. The experimental values of these properties are also included in Table VI for comparison. These benchmark calculations show a number of important trends: (1) decreasing the basis set quality leads to underestimation of the dipole moment and the O–Zr–O bond angle; (2) the Hartree–Fock (RHF) method with larger basis sets (3-21G+, LANL2DZ, and LANL2DZ+) predicts a correct Zr–O bond distance, but overestimates the  $\text{ZrO}_2$  dipole moment and the O–Zr–O bond angle; (3) the hybrid B3LYP DFT method predicts a good O–Zr–O bond angle, but the  $\text{ZrO}_2$  dipole moment is still higher than the measured value; (4) the BPW91 DFT method generates a good dipole moment; and (5) both B3LYP and BPW91 DFT methods somewhat overestimate the Zr–O bond distance.

In these studies, the BPW91 algorithm is employed as the primary calculational technique because it incorporates correlation energy that may be important for proper description of Zr–Zr bonding in  $(\text{ZrO}_2)_n$  clusters. Since the 3-21G+, LANL2DZ, and LANL2DZ+ basis sets give similar results, the LANL2DZ effective core potentials (ECPs) and basis sets are employed throughout these studies as a compromise between computational accuracy and cost. Optimization of a single isomer of  $(\text{ZrO}_3)_6$  at this level of theory with GAUSSIAN 98 running on a workstation benchmarked at 275 Linpack DP Mflops requires about 1 week.

Cluster geometry for  $(\text{ZrO}_2)_n$ ,  $n=3-6$ , is determined.

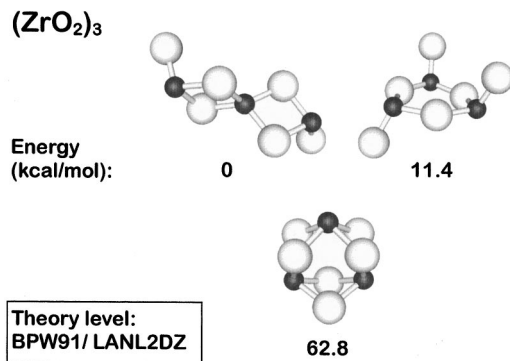


FIG. 10. Calculated structures of the various isomers of  $(\text{ZrO}_2)_3$  along with their relative energies (in kcal/mol) obtained at the BPW91/LANL2DZ theory level (see text for details).

All geometry optimizations are performed for the cluster ground electronic state and with full relaxation of all geometric coordinates. Clusters of these sizes may have many stable isomers corresponding to different local minima on the cluster potential hypersurface. For each cluster size, geometry optimizations are performed starting from a number of initial configurations to maximize chances of finding the most stable isomer (the global minima on the cluster potential surface). This procedure also finds the low energy isomers for each cluster size. Geometry optimizations are performed for three different starting structures of  $(\text{ZrO}_2)_3$ , four structures for  $(\text{ZrO}_2)_4$ , 14 structures for  $(\text{ZrO}_2)_5$ , and five structures for  $(\text{ZrO}_2)_6$ . These initial structures involve linear and triangular  $\text{Zr}_3$  and different polyhedral skeletons of  $\text{Zr}_4$ ,  $\text{Zr}_5$ , and  $\text{Zr}_6$ , each with a number of different reasonable configurations of oxygen atoms placed along edges, on faces or terminally bound to the apexes of the  $\text{Zr}_n$  skeleton. The  $\text{Zr}_5$  skeletons include a tetragonal pyramid, a trigonal bipyramidal, a tetrahedron with a central Zr atom, a pentagonal ring, a distorted pentagonal ring, and a chain of five Zr atoms. The  $(\text{ZrO}_2)_4$  starting structures are based on a tetrahedral  $\text{Zr}_4$  skeleton and a linear chain with four Zr atoms. Most of the  $(\text{ZrO}_2)_6$  starting structures are derived from a  $\text{Zr}_6$  octahedron. Other starting structures for  $(\text{ZrO}_2)_n$ ,  $n = 4 - 6$ , are derived from fragments of the high temperature tetragonal ( $\text{CaF}_2$ -like)

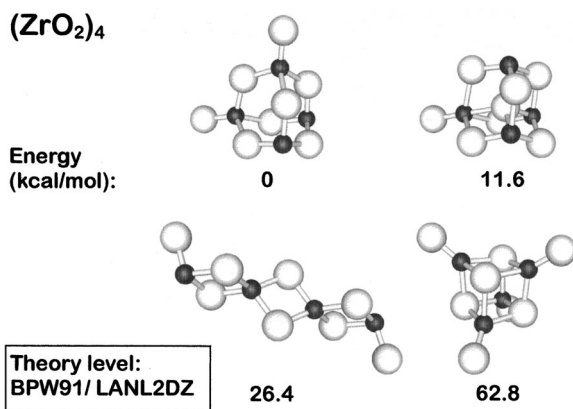


FIG. 11. Calculated structures of the various isomers of  $(\text{ZrO}_2)_4$  along with their relative energies (in kcal/mol) obtained at the BPW91/LANL2DZ theory level (see text for details).

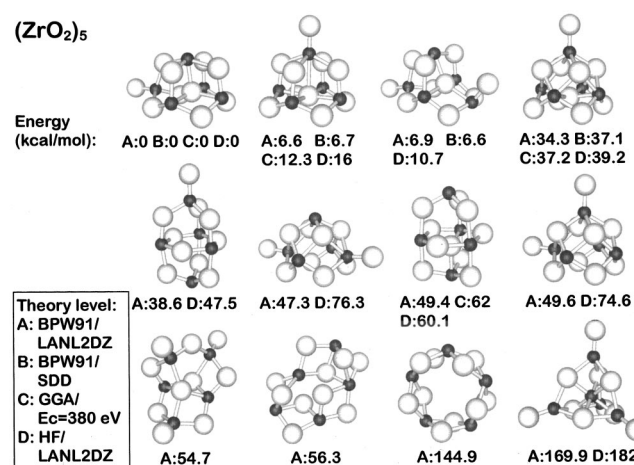


FIG. 12. Calculated structures of the various isomers of  $(\text{ZrO}_2)_5$  along with their relative energies (in kcal/mol) obtained at the BPW91/LANL2DZ theory level (see text for details). The linear isomer is not shown in order to save space.

crystalline phase of  $\text{ZrO}_2$ . Prior to each geometry optimization, the position of one atom is moved slightly to distort the starting structure symmetry. All optimization are performed with no cluster symmetry.

Figures 10–13 depict the final structures of the various isomers of  $(\text{ZrO}_2)_n$  clusters for cluster sizes  $n = 3 - 6$ , respectively, along with their total energies. The most stable  $(\text{ZrO}_2)_3$  isomer is linear with tetrahedrally coordinated Zr atoms (Fig. 10). The most stable  $(\text{ZrO}_2)_4$  isomer is a tetrahedron with four Zr atoms at the vertices, six oxygen atoms along the tetrahedron edges, and two dangling terminal (singly coordinated) oxygen atoms connected to two vertices (Fig. 11). The most stable  $(\text{ZrO}_2)_5$  isomer is a tetragonal pyramid with five zirconium atoms at the vertices, eight oxygen atoms along the edges, one oxygen atom in the pyramid plane coordinated to three zirconium atoms, and one dangling terminal oxygen atom connected to a vertex in the pyramid plane (Fig. 12).

Only two other isomers of the  $(\text{ZrO}_2)_5$  cluster are within 10 kcal/mol energy of the most stable one. The most stable  $(\text{ZrO}_2)_6$  isomer has a significantly different structure than the

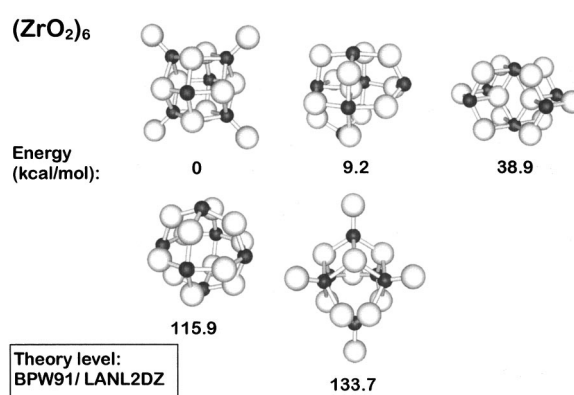


FIG. 13. Calculated structures of the various isomers of  $(\text{ZrO}_2)_6$  along with their relative energies (in kcal/mol) obtained at the BPW91/LANL2DZ theory level (see text for details).

most stable  $(\text{ZrO}_2)_5$  isomer. This globally stable  $(\text{ZrO}_2)_6$  isomer has an octahedral structure with six zirconium atoms at vertices, eight three-coordinated oxygen atoms on the faces, and four dangling terminal oxygen atoms connected to four vertices (Fig. 13). The second most stable isomer of  $(\text{ZrO}_2)_6$ , however, has oxygen atoms placed along the edges of the  $\text{Zr}_6$  skeleton; its structure is similar to the most stable isomer of  $(\text{ZrO}_2)_5$  with one  $\text{ZrO}_2$  molecule added below the tetragonal pyramid plane of  $(\text{ZrO}_2)_5$ . This similarity of structures for the most stable  $(\text{ZrO}_2)_5$  and second most stable  $(\text{ZrO}_2)_6$  isomers will be discussed below in the context of possible structural trends in the growth mechanisms for zirconium oxide clusters.

To check for possible incorrect structures for these clusters, perhaps due to the various omissions and approximations associated with the calculational approach, basis functions, or ECPs employed, the four most stable isomer structures for  $(\text{ZrO}_2)_5$  clusters obtained with LANL2DZ ECPs are subjected to recalculation and optimization with a different type of effective core potential—the Stuttgart–Dresden ECPs (potentials ECP28MWB in Ref. 16). These ECPs have a rather large basis set  $[(8s7p)$  contracted to  $[6s5p3d]]$ . Both ECP calculations yield essentially the same geometries and relative energies for the different isomers (see Fig. 12).

Additionally, to check for possible spurious results due to the basis set superposition error, structures of several  $(\text{ZrO}_2)_5$  cluster isomers are reoptimized using the Cambridge Sequential Pseudo-potential package CASTEP<sup>11</sup> running in the CERIUS 3.8 environment. In CASTEP, electron interactions are calculated by DFT. Wave functions of valence and outer core electrons are expanded in a basis of plane wave functions. The size of the basis is determined by the cutoff energy for the plane waves. The interactions of inner core electrons are described by pseudopotentials. Use of a plane wave basis set will yield a different basis set superposition error than methods in which basis functions are Gaussian functions localized on individual atomic centers. In order to employ a plane wave basis set in these calculations, the system must be periodic. Study of molecules and clusters in this regime is made possible by assuming a molecule or a cluster ion placed in a box that repeats in space. The box size must be large enough that clusters from adjacent images of the box do not interact with each other (supercell approach).

Geometry optimization by CASTEP employs the generalized gradient approximation (GGA) method. This is a DFT method employing is also referred to as the DFT gradient corrected functionals of Perdew and Wang.<sup>11,12</sup> Ultrasoft pseudopotentials (USP) of Vanderbilt and co-workers<sup>17</sup> are used for the inner core electrons. The plane wave cutoff energy is 380 eV and the cell size is 12 Å. For the  $(\text{ZrO}_2)_5$  isomers with rather compact structures, energy variations with increasing cells size become small as the cell size reaches 12 Å. The number of plane waves scales with the third power of the cell size; about 29 000 plane waves are needed for  $(\text{ZrO}_2)_5$  for these parameter values.

Six different isomeric structures for  $(\text{ZrO}_2)_5$  found by other algorithms are reoptimized using CASTEP. The final geometries are essentially the same as those found with

GAUSSIAN 98/BPW91, with the exception of the third most stable isomer obtained with GAUSSIAN 98/BPW91 (see Fig. 12). This latter isomer did not become stable at the CASTEP level and eventually collapsed to the most stable structure given in Fig. 12. The relative energies of different isomers calculated at the GGA/CASTEP theory level are within 25% of those calculated at the GAUSSIAN 98/BPW91 theory level, except for the second most stable  $(\text{ZrO}_2)_5$  isomer. The energy ordering, however, of these isomers is the same at both levels of theory; this is a very encouraging finding and gives important support to the usefulness of these qualitative results.

Finally, the eight most stable  $(\text{ZrO}_2)_5$  isomers are again reoptimized at the Hartree–Fock level of theory using GAUSSIAN 98 with LANL2DZ ECPs. The corresponding energies are shown in Fig. 12. The resulting geometries are found to be virtually identical to those obtained at the DFT level. The energy ordering of the isomers is also the same and the relative energies are similar to those for the DFT calculations except for the two high energy isomers with partially open, hollow cage structures (see Fig. 11).

Figure 14 presents the calculated total binding energies  $\text{BF}_n$  for the most stable isomers for cluster size  $n=3–6$ . The total binding energy of the  $(\text{ZrO}_2)_n$  cluster is defined as the difference between the energy of  $n$  isolated  $\text{ZrO}_2$  molecules and the energy of the  $(\text{ZrO}_2)_n$  cluster. The total binding energy can then be obtained from *ab initio* calculations as

$$\text{BE}_n = nE_1 - E_n . \quad (19)$$

The differences between the total binding energies of  $(\text{ZrO}_2)_n$  and  $(\text{ZrO}_2)_{n-1}$  give the adiabatic dissociation energy  $E_{d,n}$  of the  $(\text{ZrO}_2)_n$  cluster [i.e.,  $(\text{ZrO}_2)_n \rightarrow (\text{ZrO}_2)_{n-1} + \text{ZrO}_2$ ],

$$E_{d,n} = \text{BE}_n - \text{BE}_{n-1} , \quad (20)$$

which is a measure of the cluster stability.

The basis set superposition errors for such calculations are nonzero, but since only energy differences are calculated, one can expect them to be systematically reduced. The dissociation energies of  $(\text{ZrO}_2)_n$ ,  $n=4–6$ , are also given in Fig. 14 and tabulated in Table VII. The dissociation energy of the  $(\text{ZrO}_2)_5$  cluster is higher than that of both  $(\text{ZrO}_2)_4$  and  $(\text{ZrO}_2)_6$  clusters. In fact,  $E_{d,5}$  is almost 50% higher than  $E_{d,6}$ . This is in agreement with the experimental observation that the  $(\text{ZrO}_2)_5$  cluster is an exceptionally stable cluster in the  $(\text{ZrO}_2)_n$  neutral cluster distribution.

The second derivative of the cluster energy with respect to cluster size,

$$\Delta^2 E_n = E_{n+1} + E_{n-1} - 2E_n \quad (21)$$

is a measure of the relative abundance of the cluster with cluster size  $n$  compared to clusters with sizes  $n-1$  and  $n+1$  in the cluster distribution. The rationalization for this assertion is as follows: for thermodynamic equilibrium, the ratio of the  $(\text{ZrO}_2)_n$ ,  $(\text{ZrO}_2)_{n-1}$ , and  $(\text{ZrO}_2)_{n+1}$  cluster concentrations can be expressed as

$$\frac{[(\text{ZrO}_2)_n]^2}{[(\text{ZrO}_2)_{n-1}][(\text{ZrO}_2)_{n+1}]} = \exp\left(\frac{\Delta^2 S_n}{k} - \frac{\Delta^2 H_n}{kT}\right) . \quad (22)$$

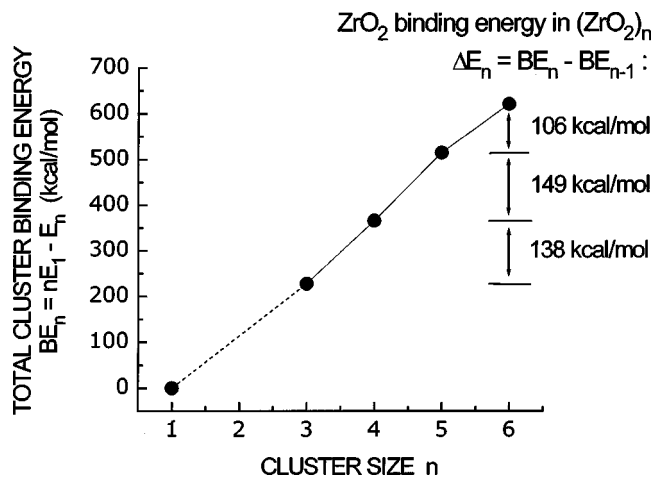


FIG. 14. The calculated total binding energy  $BE_n$  of the most stable cluster isomers as function of cluster size  $n$  for  $n=3-6$ . The total binding energy of the  $(\text{ZrO}_2)_n$  cluster is defined as the difference between energies of  $n$  isolated  $\text{ZrO}_2$  molecules and the energy of the  $(\text{ZrO}_2)_n$  cluster. Energies are obtained from *ab initio* calculations. The  $\text{ZrO}_2$  binding energy in the  $(\text{ZrO}_2)_n$  cluster,  $\Delta E_n = BE_n - BE_{n-1}$ , is also shown for  $n=3-6$  on the right-hand side of the figure.

The respective cluster concentrations are indicated with [ ] notation,  $k$  is the Boltzmann constant, and  $\Delta^2 S_n$  and  $\Delta^2 H_n$  are the second derivatives, with respect to cluster size, of the cluster entropy and enthalpy, respectively. Since  $\Delta^2 H_n \sim \Delta^2 E_n$ , under the assumption that  $\Delta^2 S_n \sim 0$ , Eq. (21) can be simplified to

$$\begin{aligned} \frac{[(\text{ZrO}_2)_n]^2}{[(\text{ZrO}_2)_{n-1}][(\text{ZrO}_2)_{n+1}]} &\approx \exp\left[\frac{\Delta^2 E_n}{kT}\right] \\ &= \exp\left[\frac{E_{d,n} - E_{d,n+1}}{kT}\right]. \end{aligned} \quad (23)$$

From Eq. (19) to Eq. (21),

$$\Delta^2 E_n = E_{d,n} - E_{d,n+1}. \quad (24)$$

The  $\Delta^2 E_n$  values for  $n=4$  and 5 are present in Table VII.  $\Delta^2 E_5$  is positive and is  $\sim 2.2$  eV higher than  $\Delta^2 E_4$ , which is negative. Structures and energies for  $(\text{ZrO}_2)_7$  clusters have not been calculated, and therefore,  $\Delta^2 E_6$  is not known; however,  $\Delta^2 E_6$  cannot be as high as  $\Delta^2 E_5$  unless  $E_{d,7}$  of  $(\text{ZrO}_2)_7$  is lower than 2.6 eV. That is,  $E_{d,7}$  would have to be less than one-half of  $E_{d,5}$ , which seems unlikely. Thus,  $\Delta^2 E_5$  is higher than  $\Delta^2 E_4$  and most likely higher than  $\Delta^2 E_6$ , which

TABLE VII. Dissociation energy,  $E_{d,n}$ , and the second derivative of the total cluster energy,  $d^2 E_n / dn^2$ , of  $(\text{ZrO}_2)_n$  clusters tabulated as functions of the cluster size  $n$ . See also Fig. 10.

Cluster size $n$	Dissociation energy		$d^2 E_n / dn^2$	
	$E_{d,n}$ $= E_{n-1} + E_1 - E_n$	(kcal/mol) (eV)	$= E_{n+1} + E_{n-1} - 2E_n$	(kcal/mol) (eV)
4	138	5.65	-11	-0.45
5	149	6.10	43	1.75
6	106	4.35		

TABLE VIII. Vertical and adiabatic ionization energies of the most stable  $(\text{ZrO}_2)_n$  cluster isomers calculated on the BPW91/LANL2DZ theory level are tabulated as functions of the cluster size  $n$ .

Cluster size $n$	Vertical ionization energy (eV)	Adiabatic ionization energy (eV)
4	7.8	7.6
5	8.3	7.7
6	9.0	8.5

means that  $(\text{ZrO}_2)_5$  is a “magic number” cluster in the neutral cluster distribution. This is consistent with the experimental observation. Table VIII compares the calculated vertical and adiabatic ionization energies for the most stable cluster isomers as a function of cluster size.

In conclusion, DFT calculations (supported by Hartree–Fock calculations) using the gradient corrected exchange functional of Becke, gradient corrected correlation functional of Perdew and Wang, LANL2DZ effective core potentials, and a valence double-zeta basis set, reproduce the experimental observation that the  $(\text{ZrO}_2)_5$  cluster is an exceptionally stable cluster in the  $(\text{ZrO}_2)_n$  neutral cluster distribution. We are thus confident that the cluster size-dependent structural trends calculated for zirconium oxide clusters are also properly described by this level of theory. These structural trends are discussed in the following section.

## V. DISCUSSION

One may expect that a “magic number” cluster in a mass spectrum is indicative of a shell closing and that it corresponds to some compact and symmetric structure, such as, for example,  $\text{C}_{60}$ ,  $\text{Ti}_8\text{C}_{12}$ , or  $\text{Ar}_{13}$ . This study shows that such an expectation is not always correct: the one dangling oxygen atom in the plane of the tetragonal pyramid makes the  $(\text{ZrO}_2)_5$  neither compact, symmetric, nor a “closed shell.” What, then, is the origin of the high stability of  $(\text{ZrO}_2)_5$ ?

The most stable isomer structures of  $(\text{ZrO}_2)_4$  (Fig. 11) and  $(\text{ZrO}_2)_5$  (Fig. 12) and the second most stable isomer of  $(\text{ZrO}_2)_6$  (Fig. 13) can be related by a simple growth pattern. This pattern is based on the sequential addition of two  $\text{ZrO}_2$  molecules to the  $(\text{ZrO}_2)_4$  cluster “nucleus.” The  $(\text{ZrO}_2)_4$  “nucleus” is slightly deformed to accommodate the new  $\text{ZrO}_2$  adduct. The entire growth sequence is presented in Fig. 15. In the first step of this process, the  $\text{ZrO}_2$  molecule is bound to the edge of a tetrahedral  $(\text{ZrO}_2)_4$  with slight deformation of the  $(\text{ZrO}_2)_4$ . One of the dangling oxygens of  $(\text{ZrO}_2)_4$  is thereby coordinated to the  $\text{ZrO}_2$  adduct, as depicted in the right-hand side of Fig. 15. This growth process step yields  $(\text{ZrO}_2)_5$ . In the second step of the  $n=4 \rightarrow n=6$  growth process,  $\text{ZrO}_2$  is attached beneath the plane of the  $(\text{ZrO}_2)_5$  tetragonal pyramid and the remaining dangling oxygen atom of the  $(\text{ZrO}_2)_4$  “nucleus” turns toward the  $\text{Zr}$  atom of the  $\text{ZrO}_2$  adduct. This second step of the growth process yields the second most stable  $(\text{ZrO}_2)_6$  isomer, not the most stable one.

Table IX gives the relative energies of the  $(\text{ZrO}_2)_4$  “nucleus” in the  $(\text{ZrO}_2)_n$ ,  $n=4-6$ , clusters. These energies

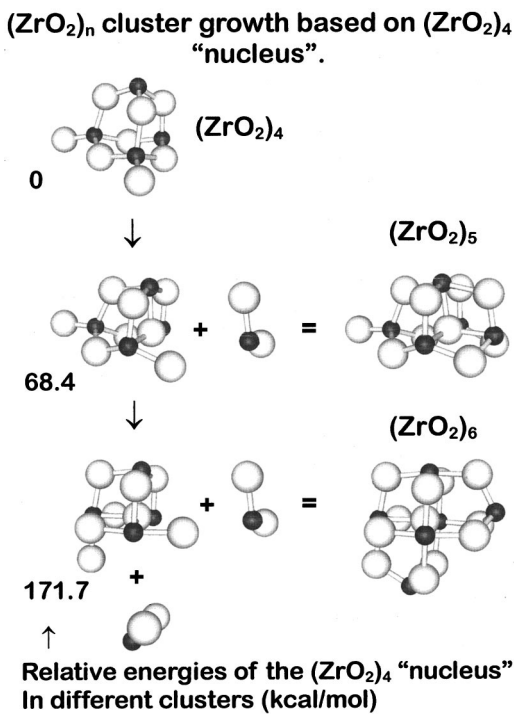


FIG. 15. Growth pattern of  $(\text{ZrO}_2)_n$ ,  $4 \leq n \leq 6$ , clusters based on addition of one and two  $\text{ZrO}_2$  molecules to the  $(\text{ZrO}_2)_4$  cluster ‘nucleus.’ Before each addition, the  $(\text{ZrO}_2)_4$  ‘nucleus’ is slightly deformed to accommodate the new  $\text{ZrO}_2$  adduct. The relative energies of the  $(\text{ZrO}_2)_4$  ‘nucleus’ in  $(\text{ZrO}_2)_n$ ,  $n = 4–6$  clusters are also shown (see text for details).

are obtained by the following procedure. For  $n = 5$ , one  $\text{ZrO}_2$  molecule is removed for the most stable  $(\text{ZrO}_2)_5$  isomer to obtain its  $(\text{ZrO}_2)_4$  ‘nucleus’ (see Fig. 15). The single point energy for this  $(\text{ZrO}_2)_4$  ‘nucleus’ is calculated and subtracted from the energy of the most stable  $(\text{ZrO}_2)_4$  isomer. For  $n = 6$ , two  $\text{ZrO}_2$  molecules are removed from the  $(\text{ZrO}_2)_6$  second most stable isomer to obtain, through a single point calculation, the energy of its  $(\text{ZrO}_2)_4$  ‘nucleus’ (Fig. 15). The energies thus obtained for  $(\text{ZrO}_2)_4$  moiety in the  $n = 5, 6$  clusters reflect how much the  $(\text{ZrO}_2)_4$  ‘nucleus’ is destabilized by deformation at each  $\text{ZrO}_2$  addition step.

Table IX shows that the second  $\text{ZrO}_2$  addition destabilizes the  $(\text{ZrO}_2)_4$  ‘nucleus’ much more than the first addition. Even though the  $(\text{ZrO}_2)_6$  second most stable isomer has no dangling oxygen atoms (which should make it more stable), it is destabilized by deformation strain of the  $(\text{ZrO}_2)_4$  building block. Thus, the ‘magic number’ nature of the  $(\text{ZrO}_2)_5$  cluster results from an interplay between stabilization of the  $(\text{ZrO}_2)_4$  cluster ‘nucleus’ by engaging its

TABLE IX. Relative energies of the  $(\text{ZrO}_2)_4$ , ‘nucleus’ in  $(\text{ZrO}_2)_n$ ,  $n = 4–6$  clusters (see text for details). See also Fig. 15.

Cluster size $n$	Relative energy of the $(\text{ZrO}_2)_4$ ‘nucleus’ in $(\text{ZrO}_2)_n$ cluster (kcal/mol)
4	0
5	68.4
6	171.7

dangling oxygen atoms through bonding with  $\text{ZrO}_2$  adducts, and destabilizing the  $(\text{ZrO}_2)_4$  ‘nucleus’ by a strain resulting from its deformation and tilting of oxygen atoms toward the adduct  $\text{ZrO}_2$ . For addition of the first  $\text{ZrO}_2$  molecule to the  $(\text{ZrO}_2)_4$  cluster, the stabilizing effect prevails over the destabilizing effect, resulting in  $(\text{ZrO}_2)_5$  being more stable than  $(\text{ZrO}_2)_4$ . For addition of a  $\text{ZrO}_2$  molecule to the  $(\text{ZrO}_2)_5$  cluster, the destabilizing effect prevails over the stabilizing effect, resulting in  $(\text{ZrO}_2)_6$  being less stable than  $(\text{ZrO}_2)_5$ .

A gap in the mass spectrum of Fig. 1 between  $(\text{ZrO}_2)_5$  and  $(\text{ZrO}_2)_8$  can be readily discerned. According to *ab initio* calculations, the most stable isomer of  $(\text{ZrO}_2)_6$  clusters has a different base structure than that of  $(\text{ZrO}_2)_4$  and  $(\text{ZrO}_2)_5$  clusters (see Fig. 13). The  $(\text{ZrO}_2)_6$  most stable structure is best described as a hollow octahedral cage with six zirconium atoms at vertices, eight oxygen atoms at faces (each coordinated to three zirconium atoms), and four dangling oxygen atoms. Based on this observation, we suggest that, at cluster size  $n = 6$ , a new building pattern for  $(\text{ZrO}_2)_n$  clusters begins. The old building pattern shown in Fig. 15 reaches its maximum stability at  $n = 5$ , and further growth is destabilized due to strain of its  $(\text{ZrO}_2)_4$  building block. The new structural pattern, starting at  $n = 6$ , reaches high stability at  $n = 8$  and 9 (see Fig. 10).

Note that this growth behavior for  $(\text{ZrO}_2)_n$  clusters resembles growth trends for carbon clusters: small clusters are linear, medium size clusters have ring structures, and large clusters have cage (fullerene) structures. Understanding these changing growth patterns for covalent clusters is important because different cluster ‘phases’ may exhibit different reactivities. For example, in  $(\text{ZrO}_2)_4$ , and  $(\text{ZrO}_2)_5$  clusters, most of the oxygen atoms are two-coordinated, whereas for  $(\text{ZrO}_2)_6$  clusters, most of the oxygen atoms are three-coordinated.  $(\text{ZrO}_2)_4$  and  $(\text{ZrO}_2)_5$  clusters are characterized by only a few single-coordinated dangling oxygen atoms (one and two, respectively). Conversely,  $(\text{ZrO}_2)_6$  has four dangling oxygen atoms, and we suggest that the number of dangling oxygens may be high for larger clusters in the growth sequence starting at  $n = 6$ . These oxygen atoms may be important for cluster reactivity because the highest occupied molecular orbitals of  $(\text{ZrO}_2)_5$  are localized along the bond between the dangling oxygen atom and the adjacent zirconium atom.

## VI. CONCLUSIONS

$(\text{ZrO}_2)_5$  is a very stable cluster in the  $(\text{ZrO}_2)_n$  neutral cluster distribution. It is about 50% more stable than the  $(\text{ZrO}_2)_6$  clusters.  $(\text{ZrO}_2)_5$  has neither a very symmetric nor a ‘closed shell’ structure.

The ‘magic’ character of the  $(\text{ZrO}_2)_5$  neutral cluster is the result of the interplay between: (1) stabilization of the  $(\text{ZrO}_2)_4$  cluster ‘nucleus’ by engaging its dangling oxygen atom in a bond with the first  $\text{ZrO}_2$  molecular adduct to generate  $(\text{ZrO}_2)_5$ ; and (2) destabilization of the  $(\text{ZrO}_2)_4$  cluster ‘nucleus’ by strain associated with tilting of the singly coordinated oxygen atoms of  $(\text{ZrO}_2)_5$  toward the second  $\text{ZrO}_2$  adduct to generate  $(\text{ZrO}_2)_6$ .

Only three low energy ( $<10$  kcal/mol) isomers of  $(\text{ZrO}_2)_5$  can be calculated. The most stable  $(\text{ZrO}_2)_6$  cluster isomer has a very different base structure from that of  $(\text{ZrO}_2)_4$  and  $(\text{ZrO}_2)_5$  clusters. For the most stable  $(\text{ZrO}_2)_6$  cluster isomer, the oxygen atom coordination numbers are 1 and 3. For the most stable  $(\text{ZrO}_2)_4$  and  $(\text{ZrO}_2)_5$  cluster isomers, the oxygen atom coordination numbers are 1 and 2.

$(\text{ZrO}_2)_6$  may be the first cluster in a new structural pattern that reaches high stability at cluster sizes  $(\text{ZrO}_2)_8$  and  $(\text{ZrO}_2)_9$ .

Modeling and simulation studies suggest that  $(\text{ZrO}_2)_n$  neutral clusters are not ionized by thermionic emission resulting from many-photon absorption by the  $(\text{ZrO}_2)_n$  neutral clusters and internal conversion "cycling" and "heating." The multiphoton ionization process probably consists of the following two steps: (1) two photons are absorbed by  $(\text{ZrO}_2)_n$  neutral clusters to create  $(\text{ZrO}_2)_n$  ions; and (2) several more photons are absorbed by the cluster ions potentially leading to cluster ion fragmentation. At low ionization laser intensity, cluster ion absorption is probably greatly reduced or absent, thereby greatly reducing the extent of cluster ion fragmentation.

## ACKNOWLEDGMENTS

These studies are partially supported by grants from the U.S. National Science Foundation and the Army Research Office.

- <sup>1</sup>(a) G. A. Somorjai, *Surface Chemistry and Catalysis* (Wiley, New York City, 1994); (b) R. I. Masel, *Adsorption and Reaction on Solid Surfaces* (Wiley, New York City, 1996); (c) P. A. Cox, *Transition Metal Oxides* (Oxford, New York City, 1992); (d) V. E. Henrich, P. A. Cox, *Surface Science of Metal Oxides* (Cambridge, New York City, 1994).
- <sup>2</sup>(a) Y. Shi and K. M. Ervin, *J. Chem. Phys.* **108**, 1757 (1998); (b) G. Ertl and H. J. Freund, *Phys. Today* Jan., 32 (1999), and references therein; (c) W. D. Vann, R. L. Wagner, and A. W. Castleman, Jr., *J. Phys. Chem. A* **102**, 1708 (1998); (d) **102**, 8804 (1998); (e) R. C. Bell, K. A. Zemski, and A. W. Castleman, Jr., *ibid.* **103**, 1585 (1999); (f) W. D. Vann and A. W. Castleman, Jr., *ibid.* **103**, 847 (1999); (g) D. Schröder and H. Schwarz, *Angew. Chem. Int. Ed. Engl.* **34**, 1973 (1995); (h) K. Eller and H. Schwarz, *Chem. Rev.* **91**, 1121 (1991).
- <sup>3</sup>(a) S. J. Riley, in *Metal Ligand Interactions: From Atoms to Clusters to Surfaces*, edited by D. R. Salahub and N. Russo (Kluwer, Dordrecht, 1992), pp. 17–36; (b) G. C. Nieman, E. K. Parks, S. C. Richtsmeier, K. Liu, L. G. Pobo, and S. J. Riley, *High. Temp. Sci.* **22**, 115 (1986); (c) E. K. Parks, B. J. Winter, T. K. Klots, and S. J. Riley, *J. Chem. Phys.* **94**, 1992 (1991); (d) H. T. Deng, K. P. Kerns, and A. W. Castleman, Jr., *ibid.* **100**, 13386 (1996); (e) X. Lu, X. Xu, N. Q. Wang, Q. Zhang, M. Ehara, and H. Nakatsuji, *Chem. Phys. Lett.* **291**, 445 (1998); (f) K. A. Zemski, R. C. Bell, and A. W. Castleman, Jr., *J. Phys. Chem. A* **104**, 5732 (2000).

- <sup>4</sup>(a) G. M. Koretsky, K. P. Kerns, G. C. Nieman, M. B. Knickelbein, and S. J. Riley, *J. Phys. Chem. A* **103**, 1997 (1999); (b) M. B. Knickelbein, *Philos. Mag. B* **79**, 1379 (1999); (c) M. B. Knickelbein, *Annu. Rev. Phys. Chem.* **50**, 79 (1999); (d) D-S. Yang and P. A. Hackett, *J. Electron Spectrosc. Relat. Phenom.* **106**, 153 (2000); (e) D-S. Yang, M. Z. Zgierski, D. M. Rayner, P. A. Hackett, A. Martinez, D. R. Salahub, P-N. Roy, and T. Carrington, Jr., *J. Chem. Phys.* **103**, 5335 (1995); (f) K. Athanassenas, D. Kreisle, B. A. Collings, D. M. Rayner, and P. A. Hackett, *Chem. Phys. Lett.* **213**, 105 (1993); (g) P. A. Hackett, S. A. Mitchell, D. M. Rayner, and B. Simard, in *Metal–Ligand Interactions*, edited by N. Russo and D. R. Salahub (Kluwer, Dordrecht, 1996), pp. 289–324; (h) K. Athanassenas, D. Kreisle, B. A. Collings, D. M. Rayner, and P. A. Hackett, *Chem. Phys. Lett.* **213**, 105 (1993); (i) J. M. Parnis, S. A. Mitchell, T. S. Kanigan, and P. A. Hackett, *J. Phys. Chem.* **93**, 8045 (1989); (j) S. Matt, O. Echt, M. Sondergger, R. David, P. Scheier, J. Laskin, C. Lifshitz, and T. D. Mark, *Chem. Phys. Lett.* **303**, 379 (1999); (k) J. M. Parnis, R. D. Lafleur, and D. M. Rayner, *Chem. Phys. Lett.* **218**, 544 (1994).
- <sup>5</sup>(a) D. van Heijnsbergen, G. von Helden, M. A. Duncan, A. J. A. van Roij, and G. Meijer, *Phys. Rev. Lett.* **83**, 4983 (1999); (b) A. W. Castleman, Jr. and K. H. Bowen, Jr., *J. Phys. Chem. A* **100**, 12911 (1996); (c) M. S. Dresselhaus, G. Dresselhaus, and P. C. Eklund, *Science of Fullerenes and Carbon Nanotubes* (Academic, New York City, 1996).
- <sup>6</sup>(a) M. Foltin, G. Stueber, and E. R. Bernstein, *J. Chem. Phys.* **111**, 9577 (1999); (b) **109**, 4342 (1998). References to the older literature on covariance mapping can be found in these references.
- <sup>7</sup>(a) B. A. Collings, A. H. Amrein, D. M. Rayner, and P. A. Hackett, *J. Chem. Phys.* **99**, 4174 (1993); (b) R. C. Bell, K. A. Zemski, and A. W. Castleman, Jr., *J. Cluster Sci.* **10**, 509 (1999).
- <sup>8</sup>K. P. Huber and G. Herzberg, *Molecular Spectra and Molecular Structure: Constants of Diatomic Molecules* (van Nostrand Reinhold, New York City, 1979).
- <sup>9</sup>R. D. Levin and S. G. Lias, *Natl. Stand. Ref. Data Ser. (U.S., Natl. Bur. Stand.)* **71**, 484 (1982); see also E. G. Rauh and R. J. Ackerman, *J. Chem. Phys.* **60**, 1396 (1974).
- <sup>10</sup>M. J. Frisch, G. W. Trucks, H. B. Schlegel *et al.*, *GAUSSIAN 98*, Revision A.6, Gaussian, Inc., Pittsburgh, PA, 1998.
- <sup>11</sup>Molecular Simulations, Inc.
- <sup>12</sup>(a) K. Burke, P. J. Perdew, and Y. Yang, in *Electronic Density Functional Theory: Recent Progress and New Directions*, edited by J. F. Dobson, G. Vignale, and P. M. Das (Plenum, New York City, 1998); (b) J. P. Perdew, in *Electronic Structure of Solids*, edited by P. Ziesche and H. Eschrig (Akademie Verlag, Berlin, 1991), p. 11; (c) J. P. Perdew, J. A. Chevary, S. H. Vosko, K. A. Jackson, M. R. Pederson, D. J. Singh, and C. Fiol Hais, *Phys. Rev. B* **46**, 6671 (1992); **48**, 4978 (1993); (d) J. P. Perdew, K. Burke, and Y. Wang, *ibid.* **54**, 16533 (1996).
- <sup>13</sup>A. D. Becke, *J. Chem. Phys.* **104**, 1040 (1996).
- <sup>14</sup>P. J. Hay and W. R. Wadt, *J. Chem. Phys.* **82**, 270 (1985); **82**, 284 (1985); **82**, 299 (1985).
- <sup>15</sup>D. J. Brugh, R. D. Suenram, and W. J. Stevens, *J. Chem. Phys.* **111**, 3526 (1999).
- <sup>16</sup>D. Andrae, V. Haeussermann, M. Dolg, H. Stoll, and H. Preuss, *Theor. Chim. Acta* **77**, 123 (1990).
- <sup>17</sup>(a) D. Vanderbilt, *Phys. Rev. B* **41**, 7892 (1990); (b) G. Kresse and J. Hafner, *J. Phys.: Condens. Matter* **6**, 8245 (1994); (c) K. Laasonen, A. Pasquarello, R. Car, C. Lee, and D. Vanderbilt, *Phys. Rev. B* **47**, 10142 (1993); (d) A. Pasquarello, K. Laasonen, R. Car, C. Lee, and D. Vanderbilt, *Phys. Rev. Lett.* **69**, 1982 (1992).